TriDurLE

National Center for Transportation Infrastructure Durability & Life-Extension

Project ID: 2020-MST-04

NUMERICAL SIMULATION OF PAVEMENT INSTALLED WITH WICKING GEOTEXTILE IN RESPONSES TO CLIMATIC CONDITIONS

Final Report

By

Chuang Lin, Ph.D.
Missouri University of Science and Technology

Xiong Zhang, Ph.D., P.E.
James A. Heidman Professor of Civil Engineering
Missouri University of Science and Technology

for

National University Transportation Center TriDurLE
Department of Civil & Environmental Engineering
405 Spokane Street, PO Box 642910
Washington State University, Pullman, WA 99164-2910

November 15, 2022

Publication Report Option

The work in this research was summarized as two technical papers, which have been accepted for publication in *ASCE's Journal of Transportation Engineering, Part B: Pavements* and formatted in the style used by the National Center for Transportation Infrastructure Durability & Life-Extension (TriDurLE).

Acknowledgements

This project was partially supported by Geosynthetic Institute Fellowship to the first author and the materials presented in this report was provided by TenCate Geosynthetics Americas. The authors appreciate their support.

Disclaimer

Table of Contents

List of Figures

List of Tables

Executive Summary

The seasonal variation of unbound material properties is often significant and water within a pavement structure is a principal cause of pavement deterioration. A small water content increment will result in a significant reduction in soil resilient moduli and a tremendous increment in permanent deformation. Unfortunately, the resilient modulus determined by falling weight deflectometer tests may not be representative and the conventional enhanced integrated climatic model has its own limitations. This study aims at numerically simulating the seasonal variations of the resilient behavior of a base course under saturated/unsaturated conditions with the influence of localized climatic conditions. A coupled hydro-mechanical model with considerations of climatic effect was proposed and calibrated. Then, three case studies were conducted to evaluate the dynamic resilient behavior of the base course under different climatic and working conditions. The suction, water content, and resilient modulus distributions were presented to demonstrate the dynamic resilient behavior of the base course and the advantages of the proposed model against the EICM in terms of simulating the moisture migration within pavement structures are discussed.

Chapter. 1 Introduction

1.1 Problem Statement

H2Ri is a multi-functional geosynthetic product manufactured by TenCate Geosynthetics to provide drainage, reinforcement, and separation functions simultaneously. By installing a layer of wicking fabric horizontally in a pavement, both gravity and capillary water can be absorbed from the soil, transported along the wicking fabric to the shoulder, and vaporize to the surrounding atmosphere. When water is removed and soils are kept relatively dry, the pavement performance will be significantly improved. This concept has been proven through laboratory tests and validated by several field applications such as the Beaver Slide of the Dalton Highway, Dalton Highway 197-209 Experimental Feature project, Parks Highway project, etc.

The collaborative laboratory research performed at the University of Kansas has quantified the short-term benefits of H2Ri. However, the short-term lab test lasted for a very limited period was performed under a controlled laboratory condition, which may not reflect the H2Ri full benefits in the field climatic conditions in the long run. In addition, it is very difficult, if not impossible, to quantify / separate the multiple benefits of the H2Ri wicking fabric as drainage, and reinforcement material through laboratory model tests for several reasons: (1) laboratory tests are laborious, costly, and time consuming. It is not possible for us to exhaust all possible combinations of test conditions; (2) the soil-wicking fabric interaction could be coupled together and be highly nonlinear. As a result, we cannot simply superimpose the individual benefit effects together; (3). Some tests are physically impossible to run. For example, designers often questioned that (1) what is the benefits of wicking alone on the performance of pavement? (2) How much and how fast the water can be drained under local climatic conditions? (3) How many layers of wicking fabric should be installed and where is the optimum location to install the H2Ri wicking fabric? Answers to these questions are important to provide the design method for H2Ri and attract more extensive use of the H2Ri wicking fabric.

At present, there is still no design method to take full advantage of the benefits of H2Ri wicking fabric and all designs are purely based on engineer’s judgement. Currently TenCate uses the AASHTO 1993 pavement design guide to incorporate high-strength geosynthetics into pavement design, however, the benefits of H2Ri unique wicking property are not considered. Moreover, it is not cost and time effective to perform field tests to assess the H2Ri wicking fabric long-term performance under different climatic conditions.

On the other hand, numerical simulation is a feasible and economic way to test and quantify the H2Ri benefits in terms of pavement design under different climatic conditions and stages during its service life. The proposed research will be divided into several tasks to further understand the H2Ri working mechanism under field conditions, and to quantify the H2Ri benefits into existing pavement design. Firstly, the required inputs for numerical simulation will be collected and calibrated based on previous lab tests performed at the University of Alaska Fairbanks. This study includes summarizing and calibrating both the soil and H2Ri mechanical and hydraulic properties based on lab elemental and full-scale test results. Secondly, a hydro-mechanical model will be proposed to simulate the climate-plant-unsaturated soil infrastructure interaction. This model will also be calibrated using localized climatic data, such as wind speed, precipitation, solar radiation, relative humidity, etc. Thirdly, the calibrated model will be used to simulate the H2Ri performance under different conditions that it may encounter in the field. The H2Ri performance will be tested during and after rainfall events, with vegetation coverage, and with/without crack propagations (depends on the pavement condition). After that, additional “numeric tests” will be performed on “virtual” wicking fabric with varied wicking and reinforcement ability to better understand the individual and combined benefits of the wicking fabric. Last but not the least, the comprehensive simulation results will be used to incorporate the H2Ri drainage benefits into existing pavement designs (both AASHTO and MEPDG) to quantify the benefits in terms of effective roadbed resilient moduli, structural layer coefficient and drainage coefficient.

1.2 Objectives and Scope

This proposed research has the following objectives:

1. to develop and calibrate a coupled hydro-mechanical model with considerations of climatic effect.
2. to predict the dynamic resilient behavior of a base course and the interactions among the soil mass, vegetation, and the ambient environment.
3. to demonstrate the dynamic resilient behavior of the base course and the advantages of the

proposed model against the EICM in terms of simulating the moisture migration within pavement structures.

1.3 Report Overview

This report includes six chapters and a list of references. Chapter 1 presents an introduction of the study and the scope of the work. Chapter 2 provided a thorough literature review on seasonal variations of resilient modulus of the base course. In Chapter 3, a coupled hydro-mechanical model with considerations of climatic effect was proposed. The proposed model was calibrated in Chapter 4. Then, three case studies were conducted to evaluate the dynamic resilient behavior of the base course under different climatic and working conditions in Chapter 5. Finally, the summary and conclusions of the study are presented in Chapter 6.

Chapter. 2 Literature Review

The seasonal variation of unbound material properties is often significant and water within a pavement structure is a principal cause of pavement deterioration (Miller 1953). Christopher et al. (2010) showed that the initial construction cost of a flexible pavement may increase by 44% per lane-kilometer as a consequence of poor drainage. Excess water can also decrease the resilient modulus and shear strength, resulting in pavement degradations (Roberson and Siekmeier 2002). For example, when soil water content increased from 3.3% to 6%, the resilient modulus for Alaska D-1 base course aggregate reduced by 50% and the permanent deformation was doubled or even tripled (Li et al. 2011). Moreover, government transportation engineers in cold regions credited a minimum of half of road maintenance expenditures to the effect of freezing and thawing (Henry and Holtz 2001), which was another common water-related hazard occurred in northern regions of the United States.

Both the AASHTO (1993) and Mechanistic-Empirical Pavement Design Guide (MEPDG) (ARA 2004) design methods include provisions for including seasonal variations of unbound material properties. ASTM D420-18 (2018) provides detailed procedures for performing geotechnical site characterizations. Coring and sampling are a major destructive test which has many limitations, particularly when conducted on moderate or heavily trafficked highway systems. Moreover, the practical restraints, in terms of money and time, severely limit the number and variety of destructive tests conducted on routine pavement evaluation studies (AASHTO 1993; Shahin 1994). In comparison, the nondestructive test (NDT) becomes more popular since this type of examination of pavement structure does not cause damage or property changes to the structure. Among all NDT testing techniques, the FWD (Falling Weight Deflectometer) test is one of the most reliable ways of determining the in-situ moduli of the pavement system (ARA 2004). It can be used to determine the variations of the pavement layer and the resilient modulus of each layer can be back-calculated given the thickness of each layer (ASTM D4694-09 2015). An accurate prediction of the resilient modulus value is important since it is a required input to the structural response computation model in both AASHTO 1993 and MEDPG approaches. However, the resilient modulus values back-calculated from the FWD test are highly dependent on the ambient climatic conditions, such as the depth of groundwater table, the intensity, and duration of precipitation, and solar radiation, etc. The FWD test is normally conducted on a bi-weekly or monthly basis (Huang 2004; ARA 2004) and the back-calculated resilient modulus values represent the particular values at that moment of the year, which may not be a representative value for the entire month or season. It is necessary to come up with an accurate approach to predict the resilient behavior of a base course under localized climatic conditions.

The AASHTOWare Pavement ME Design software is the production version of the MEPDG and can provide reasonable predictions of seasonal variations of resilient modulus for different pavement layers based upon the climatic data from the LTPP (Long Term Pavement Performance) and in the test section of SMP (Seasonal Monitoring Program) (Witczak et al. 2000). The climatic effects are considered in the software through the EICM (Enhanced Integrated Climatic Model) (Larson and Dempsey 1997). The EICM model integrated three separate models addressing different aspects of climatic effects on the pavement into a single comprehensive package (Richter 2006), including the CMS (Climatic-Material-Structures) model (Dempsey et al. 1985), the ID (Infiltration and Drainage) model (Liu and Lytton 1985), and the CRREL Frost Heave and Thaw Settlement Model (Guymon et al. 1986). However, the EICM model has its own limitations and still needs to be improved in several aspects. Firstly, the EICM model is a 1D model (ARA 2004), which is not accurate to evaluate the soil moisture content distributions in a 2D or 3D space. For example, the amplitude of soil moisture content variations at the center of the road must be lower than that for the soil at the edge of the road since the soils at the edge are exposed to the ambient environment and will be significantly affected by the climatic conditions. Secondly, the infiltration water determined by the EICM model is merely based upon empirical judgment. In the MEDPG approach, infiltration is assumed to be four levels: none, minor, moderate, and extreme, corresponding to 0%, 10%, 50%, and 100% of precipitation enters the pavement (ARA 2004). In reality, the infiltration rate shall be a function of both precipitation and the water storage capacity of the top unbounded layer. For example, if the top of the unbounded layer is already saturated and cannot absorb any water, the rest of the precipitation water shall be considered as runoff water rather than continuously enters into the pavement foundation. Thirdly, the drainage model in EICM, also known as DRIP (Drainage Requirements in Pavements) (Wyatt et al. 1998) model, is based upon the water flow through saturated soils and is not suitable for unsaturated conditions. The soil within a pavement structure is often compacted at the optimum water content to achieve the maximum dry density and the best performance. The soils are under unsaturated conditions during most of the time in its service life. Obviously, the DRIP model cannot accurately simulate the moisture migration within the pavement structure. Last but not least, the slopes of the road embankment are often covered with vegetation for protection, erosion control, and decoration purposes (Fredlund et al. 2012). The EICM model is not able to simulate the dynamic interactions between the soil infrastructure and vegetation under different climatic conditions.

This study aims at numerically simulating the seasonal variations of the resilient behavior of a base course under saturated/unsaturated conditions with different climatic conditions. A coupled hydro-mechanical model with considerations of climatic effect was first proposed. A finite element method (FEM) software Abaqus (Abaqus 2014) was used to evaluate the seasonal variations of base course resilient behavior according to daily meteorological data, such as relative humidity (RH), air temperature, wind speed, solar radiation, and precipitation. Then three case studies were conducted to predict the dynamic resilient behavior of a base course and the interactions among the soil mass, vegetation, and the ambient environment.

Chapter. 3 Finite Element Model

3.1 Governing Equations

Biot (1941) firstly derived the 3D coupled consolidation theory for unsaturated soils with occluded air bubbles. Fredlund and Morgenstern (1976) proposed the constitutive relations for the volume change in unsaturated soils with a continuous air phase using two stress state variables. Zhang et al. (2005) reexamine the physical meanings of the parameters used in Fredlund and Morgenstern's paper and proposed a new set of differential equations for solving the coupled consolidation problem for saturated-unsaturated soils by using a thermodynamic analogue. For engineering applications, the base course was under unsaturated conditions during most of the time in its service life. However, it might also be fully saturated during heavy rainfall events. Therefore, this research adopted Zhang's equation to evaluate pavement performance in terms of water content and resilient modulus variations, as expressed in Equation 1.

$$\left(\lambda+G\right)\frac{\partial\varepsilon_v}{\partial x}+G\nabla^2 u-\left(3\lambda+2G\right)\alpha\frac{\partial\left(-u_w\right)}{\partial x}+X=0 \tag{1a}$$

$$\left(\lambda+G\right)\frac{\partial\varepsilon_v}{\partial y}+G\nabla^2 v-\left(3\lambda+2G\right)\alpha\frac{\partial\left(-u_w\right)}{\partial y}+Y=0 \tag{1b}$$

$$\left(\lambda+G\right)\frac{\partial\varepsilon_v}{\partial z}+G\nabla^2 w-\left(3\lambda+2G\right)\alpha\frac{\partial\left(-u_w\right)}{\partial z}+Z=0 \tag{1c}$$

$$\frac{1}{\gamma_w}\left(\frac{\partial}{\partial x}(k\frac{\partial\left(-u_w\right)}{\partial x})+\frac{\partial}{\partial y}(k\frac{\partial\left(-u_w\right)}{\partial y})+\frac{\partial}{\partial z}(k\frac{\partial\left(-u_w\right)}{\partial z}+1)\right)=m_1^w\frac{\partial\sigma_m}{\partial t}+m_2^w\frac{\partial\left(-u_w\right)}{\partial t}+S \tag{1d}$$

where, *u*, *v*, and *w* = displacements in the x, y, and z directions; X, Y, and Z = body forces in the x, y, and z directions; G = shear modulus; λ = Lame constant; α = coefficient of expansion due to pore water pressure variations; ε_v = volumetric strain; u_w = pore water pressure; σ_m = mean stress; γ_w = unit weight of water; k = coefficient of permeability (assuming an isotropic soil property); t = time; m_1^w = coefficient of pore-water volume change due to the change in mechanical stress; m_2^w = coefficient of pore-water volume change due to the change in pore water pressure, $m_2^w = \rho_d C_w$; ρ_d = soil dry density; C_w = specific water capacity, or the slope of the soil water characteristic curve (SWCC); and S = water generation term, s^{-1}.

Equation 1a-c are the equilibrium equations in terms of displacements in the x, y, and z directions. Equation 1d is the water continuity equation. For Equation 1d, the value m_1^w is much smaller compared with the m_2^w and S terms. Therefore, m_1^w assumes to be zero for preliminary simulations. The last term, *S*, is the water source term which depends upon the ambient climatic conditions. How to quantify the value of S and evaluate the soil-climate interactions will be discussed in the following section. For engineering practice, mechanical stress and pore water pressure are two major factors that will influence the soil volume change, and other factors such as soil temperature, pore air pressure, and salt concentration can be considered as constants during the numerical analysis (Zhang and Liu 2008).

3.2 Climatic Effect

Unlike classical soil mechanics which deals with water head type of boundary conditions (or Dirichlet boundary conditions), the ground surface relies on a moisture flux boundary condition (or Neumann boundary conditions) which interacts with the ambient atmospheric environment (Wilson et al. 1994). The ground surface boundary conditions must be described in terms of moisture flux so that the moisture exchange between the saturated/unsaturated soil and the surrounding environment can be quantified. The roadway embankment is always hydro-seeded after construction to prevent erosion and dust contamination. Water is either entering into the pavement structure via precipitation infiltration process or leaving the pavement structure via evapotranspiration (ET) process. The precipitation infiltration process can be accurately determined given the infrastructure geometry and the local precipitation data. The evapotranspiration process can be reasonably simulated using the *FAO 56 PM* method, which was proposed by *United Nations Food and Agriculture Organization* (FAO) (Allen et al. 1998).

Soil evaporation is strongly influenced by the net radiation from the sun and the movement of air above the ground surface (Tran et al. 2015). The *FAO 56 PM* method requires measurements of air temperature, relative humidity, wind speed, and solar radiation to determine the reference evapotranspiration, as expressed in Equation 2. For this report, the field site was selected to be at Kirkwin, Kansas, and the local meteorological data of the year 2016 was obtained from WRCC (West Regional Climate Center) (WRCC 2017), as shown in Figure 1a-c. By using Equation 2, the reference evapotranspiration, ET_0, could be determined. Figure 1d shows the hourly ET_0 and precipitation data.

$$ET_0 = \frac{0.408\Delta\left(R_n - G\right) + \gamma \dfrac{900}{T+273} u_2 \left(e_s - e_a\right)}{\Delta + \gamma\left(1 + 0.34u_2\right)} \tag{2}$$

where, ET_0 = reference evapotranspiration; Δ = slope of the vapor pressure curve; R_n = net radiation at the crop surface; G = soil heat flux density, which is assumed as zero for daily calculations; γ = psychometric constant; T = mean daily air temperature at a height of 2 m; e_s and e_a = saturation and actual vapor pressure, and $(e_s - e_a)$ is the saturation vapor pressure deficit (VPD); and u_2 = wind speed at a height of 2 m.

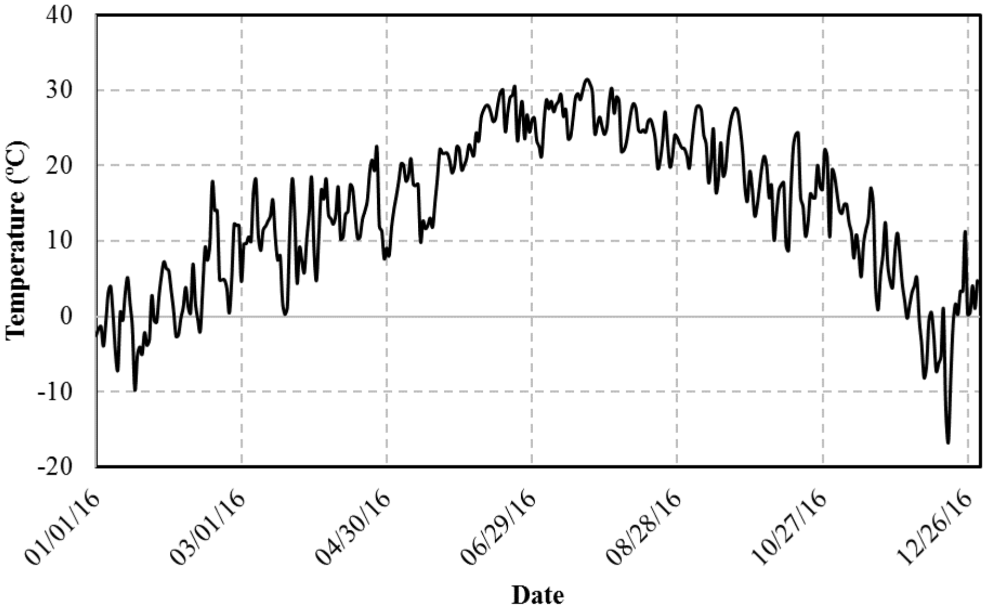

(a)

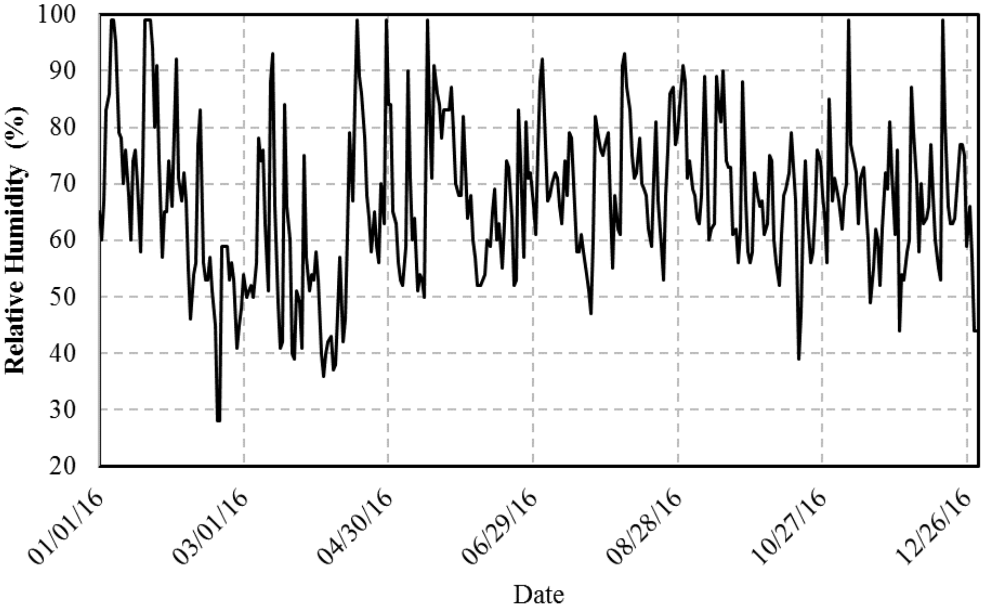
Relative Humidity (%)
100
90
80
70
60
50
40
30
20
01/01/16
03/01/16
04/30/16
06/29/16
08/28/16
10/27/16
12/26/16
Date

(b)

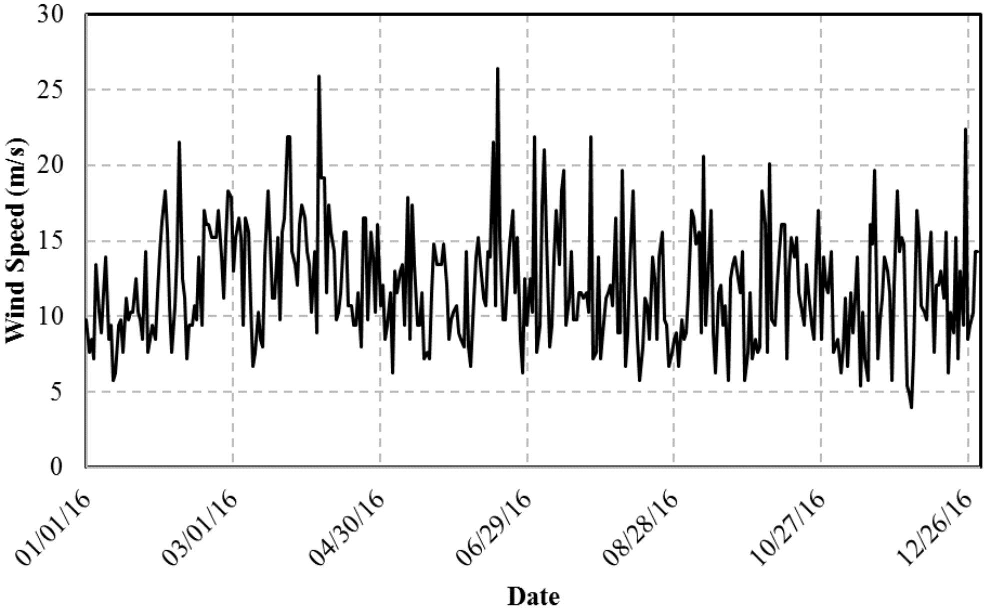
Wind Speed (m/s)
30
25
20
15
10
5
0
01/01/16
03/01/16
04/30/16
06/29/16
08/28/16
10/27/16
12/26/16
Date

(c)

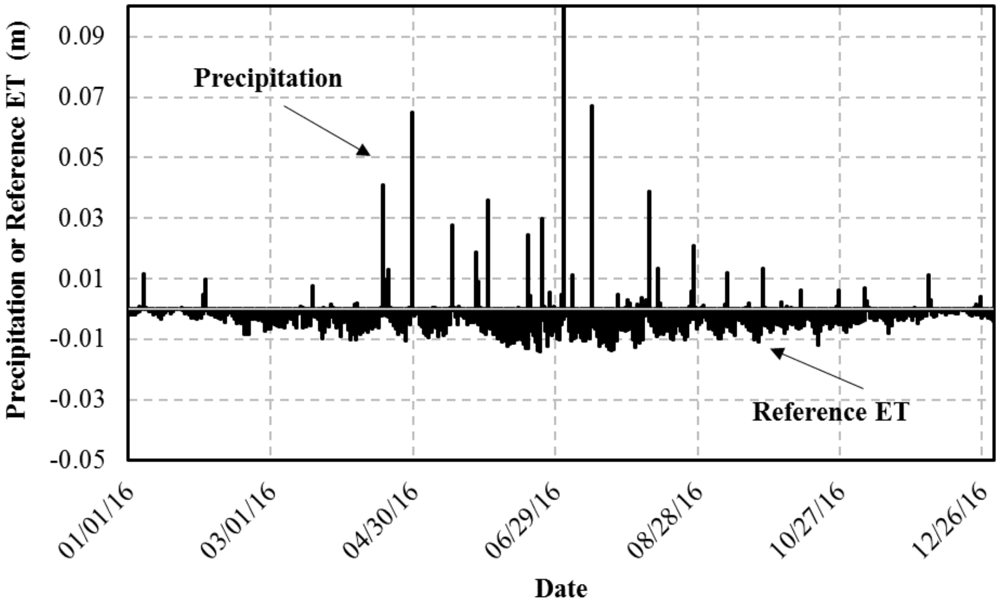

(d)

Figure 1 Meteorological data. (a) air temperature, (b) relative humidity, (c) wind speed, and (d) precipitation and calculated reference evapotranspiration.

The ET_0 gives the maximum rate of evapotranspiration under an idealized condition with a short green crop (grass), completely shading the ground, of uniform height and with adequate water status in the soil profile. The ET_0 value is only appropriate for open water or fully saturated soil surface (Wilson 1997). However, when the surface soil is in a relatively dry condition, the actual evapotranspiration (AET) rate is expected to be much smaller. The challenging part of the determination of the net infiltration is associated with accurately predicting the AET at the ground surface (Wilson et al. 1997) and it is the AET that is required for engineering modeling. Numerous researchers (Brutsaert 2013; Gray 1970; Morton 1975) have pointed out that the AET began to decline as the soil surface became unsaturated and the water supply was limited. A water balance analysis within the grass root zone would be helpful in determining the reasonable AET values, as shown in Figure 2a.

Figure 2a shows the water balance analysis of a soil element within the grass root zone. At the top surface of the soil element, the water may leave the soil via evapotranspiration process or infiltrate into the soil through the precipitation process. If the rainfall intensity was high, not all water will infiltrate into the soil element and most of the water will be considered as runoff water. Meanwhile, at the bottom of the soil element, water may also percolate to the underlying soil or wicking to the overlying soil via capillary action. Therefore, to evaluate the interactions between the soil mass and the ambient environment, it is necessary to accurately quantify the amount of water that the soil element may lose or gain. There are several critical water contents representing different soil water states and need to be defined (see in Figure 2a), namely saturation water content, field capacity (FC), threshold water content, and wilting point (WP). According to Allen et al. (1998), the total available water (TAW) represents the capacity of soil to retain water available to plants. After heavy rainfall events, water in the soil will be drained under the influence of gravity and the soil water content decreases from the saturation water content to the field capacity, which is defined as the amount of water a well-drained soil should hold against gravitational forces. As the water continued to drain and the soil water content becomes lower than the threshold value, the absence of water supply renders increasing soil stress against the water uptake by the grass and the remaining water is held to the soil particles with greater force. At this moment, not all the TAW will be available for the grass to extract, the actual amount of available water will be denoted as the readily available water (RAW), which is a fraction of the TAW. If the soil water content continued to reduce, the grass will permanently wilt if the water content is lower than the wilting point (WP). In other words, if the soil water content is lower than the wilting point, the vegetation will not survive.

The TAW is the amount of water that grass can extract from the root zone whereas the RAW is the amount of water a grass can extract from the root zone without surfer water stress. The TAW and RAW can be expressed as in Equation 3 (Allen et al. 1998):

$$TAW = (\theta_{FC} - \theta_{WP})Z_r \tag{3a}$$

$$RAW = p \times TAW \tag{3b}$$

where TAW = total available water; θ_{FC} = water content at field capacity; θ_{WP} = water content at wilting point; Z_r = grass root zone; RAW = readily available water; and p = average fraction of TAW that can be depleted from the root zone before soil stress occurs.

Based upon the TAW and RAW, the water stress coefficient, K_s, can be expressed as in Equation 4 (Allen et al. 1998):

$$K_s = \frac{TAW - D_r}{TAW - RAW} = \frac{TAW - D_r}{(1-p)TAW} \tag{4}$$

where K_s = stress coefficient; TAW = total available water; RAW = readily available water; D_r is root zone depletion; and p = average fraction of TAW that can be depleted from the root zone before soil stress occurs.

The AET is not only depended on the water stress coefficient (K_s), it also depends on the crop coefficient, K_c, which accounts for the differences in evaporation and transpiration between field crops. For geotechnical applications, the single crop coefficient approach is appropriate and an average value of 0.6 was used in this report based upon the monitored results provided by Romero and Michael (2016). Therefore, the AET is eventually a function of both stress coefficient and crop coefficient, and can be expressed as in Equation 5:

$$AET = K_s \cdot K_c \cdot ET_0 \tag{5}$$

where, AET = actual evapotranspiration; K_s = water stress coefficient; K_c = crop coefficient; and ET_0 = reference evapotranspiration.

To further demonstrate the water movement between the soil mass and the ambient environment within the grass root zone, Figure 2b presents the flow chart for the water balance analysis what is adopted in user subroutine during numerical simulations. First of all, there are several terminologies need to be defined. Assume the cross-sectional area, A, of the soil element in Figure 2a is a constant, the volume of water within the soil element can be expressed as an equivalent water height and can be expressed as in Equation 6. Meanwhile, the water stress coefficient, K_s, can also be rewritten as in Equation 7. The water source term, S, in Equation 1d can also be expressed as in Equation 8.

$$h_w = w \frac{\gamma_d}{\gamma_w} h_t \tag{6}$$

where, h_w = the equivalent water height corresponding to the current water content; h_t = equivalent height of the soil element; w = gravimetric water content; and γ_d and γ_w = unit weights of soil solids and water, respectively.

$$K_s = \frac{h_w - h_{WP}}{(1-p)(h_{FC} - h_{WP})} \tag{7}$$

where, K_s = water stress coefficient; h_w = equivalent water height; p = average fraction of TAW that can be depleted from the grass root zone before soil stress occurs; and h_{FC} and h_{WP} = equivalent water height corresponding to field capacity and wilting point, respectively.

$$S = \frac{\dot{V}_{ANWL}}{V} = \frac{ANWL \times A}{h_t \times A} = \frac{ANWL}{h_t} \tag{8}$$

where, S = water source term (per unit time); $\dot{V}_{ANWL}$ = rate of the volume of water change in the soil element; V = total volume of the soil element; h_t = equivalent height of the soil element; $ANWL$ = actual net water loss per equivalent height of soil element per unit time; and A = cross-sectional area of the soil element.

In total, there are three inputs that will be passed to the subroutine at the beginning of each time step, including the precipitation (Rain), ET (determined by Equation 2), and the suction value (a field variable that was stored at the end of the previous time step). Firstly, the actual water stress coefficient, AKS, was determined based upon Equation 4, and the actual evapotranspiration, AET, was calculated according to Equation 5. Then, the actual net water loss (ANWL) value was calculated based upon the water balance analysis shown in Figure 2a. If the $ANWL \geq 0$, the soil element is essentially losing water and there shall be no runoff water. The water source term, S, is determined based upon the comparison of the values for $ANWL$ and $(h_w - h_{WP})$. The $ANWL$ term indicates the calculated net water loss while the $(h_w - h_{WP})$ term indicates the maximum available amount of water could be lost in the soil. If the $ANWL \geq (h_w - h_{WP})$, the soil element cannot provide sufficient water to be evaporated and the water source term shall be determined based upon the value of $(h_w - h_{WP})$. On the other hand, if the $ANWL < (h_w - h_{WP})$, the water source term shall be calculated based upon the $ANWL$ term.

In comparison, if *ANWL* < 0, water is expected to flow into the soil element and the rainfall event dominates the water balance analysis. Similarly, the $(h_{sat} - h_w)$ term indicates the maximum amount of water the soil can absorb and the $(Rain - Percolation - AET)$ term represents the calculated amount of water flowing into the soil element. If $(h_{sat} - h_w) \geq$ *(Rain – Percolation – AET),* the soil element can absorb all the amount of water and the source term shall be calculated based upon the calculated value of *(Rain – Percolation – AET)*. However, if $(h_{sat} - h_w)$ < *(Rain – Percolation – AET),* the soil element cannot absorb the entire amount of water and the amount of runoff water shall be the difference between the two terms. Finally, the terms of S , ANWL, Runoff, AET, Rain, Percolation, and AKS will be stored as solution dependent variables for future usage.

3.3 Model Validation

The laboratory test performed by Leung et al. (2015) was used as a reference to calibrate the proposed numerical model. Figure 3a shows the schematic plot of the laboratory test setup. The test box was cubical with dimensions of 0.3 m × 0.3 m × 0.3 m. The thickness of the soil layer was 0.28 m with four soil suction sensors installed at elevations of 0.07 m, 0.14 m, 0.20 m, and 0.25 m, respectively. The rainfall simulator was installed on top of the test box. During the infiltration test, the ponding water on the soil surface could be drained out through the opening located at the left side of the wall so that no excess water pressure will be generated. In addition, a fluorescent lamp was also placed above the test box to provide solar radiation to the plant with an average rate of potential evapotranspiration of 2.94 mm/day. The soil was classified as clayey sand with gravel (SC) according to the Unified Soil Classification System (USCS). The plastic limit and liquid limit of the fines were 26% and 44%, respectively. The target dry density of the soil was 1.496 Mg/m^3 (80% relative compaction) and the saturated permeability was 5.79×10^{-8} m/s. The vegetation type was selected to be Schefflera heptaphylla (also known as Ivy tree) with an average root depth of 0.1 m.

For the model validation, only the drying test was used to calibrate the model. During the drying test, the readings from the four suction sensors at the beginning of the test were used as the initial condition and a constant ET value of 1.225×10^{-4} m/hour (Rain=0 during the drying test) was used as the external input (refer to Figure 2b) for the water balance analysis. The numerical model simulated the entire 12-hour drying period and the suction distribution at the end of the simulation was extracted to be compared with the laboratory test results, as shown in Figure 3b. The dash lines represent the laboratory test results for the initial and final suction distributions. The solid lines represent the suction distributions at the end of the drying test based on the proposed model by the authors and from Leung et al. (2015). At the starting point of the drying test (right after the wetting test), the soil with an elevation greater than 0.15 m had smaller suction values, indicating that this part of the soil was relatively wet compared with the underlying soil. After 12 hours of the drying process, the evapotranspiration process took out the water from the soil surface, resulting in higher suction value at an elevation of 0.28 m. Meanwhile, the water continued to percolate to the underlying soil and the soil suctions continued to decrease for soils with elevations between 0.07 m and 0.20 m. However, for soils lower than 0.07 m, the waterfront has not reached this point and the suction distribution remained constant after 12 hours. For the simulation result provided by Leung et al. (2015), it significantly deviated from the laboratory test results and their model could not catch the phenomena of the increasing suction at the top of the soil due to the imposed solar radiation boundary. In comparison, the simulation results based upon the authors' proposed model reasonably matched with the laboratory test results. The effect of the evapotranspiration on the soil suction distribution was observed in both the laboratory test and simulation results (the top 0.2 m soil). However, the simulated suction values between 0.07 and 0.20 m were higher than the laboratory test results, indicating that the provided soil permeability in the reference was lower than the actual value, and the excess water did not percolate to the underlying soil. In sum, the simulation results of the proposed FEM model matched well with the laboratory test results and the simulation results could be more accurate when given reasonable soil permeability data.

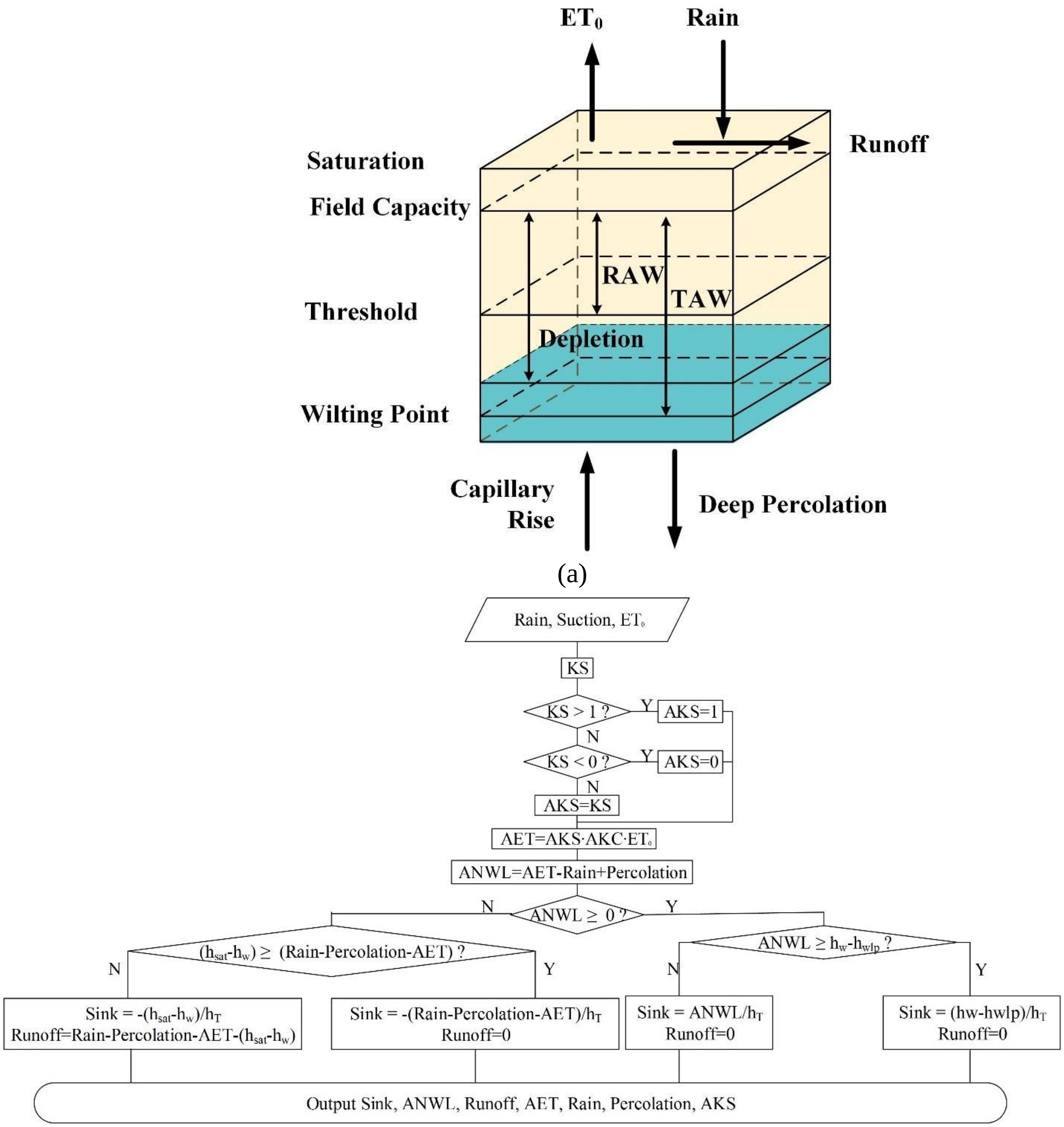

(a)

(b)

Figure 2 Water balance analysis for soil-climatic interactions. (a) schematic plot of water balance in a soil element, and (b) water balance analysis flow chart.

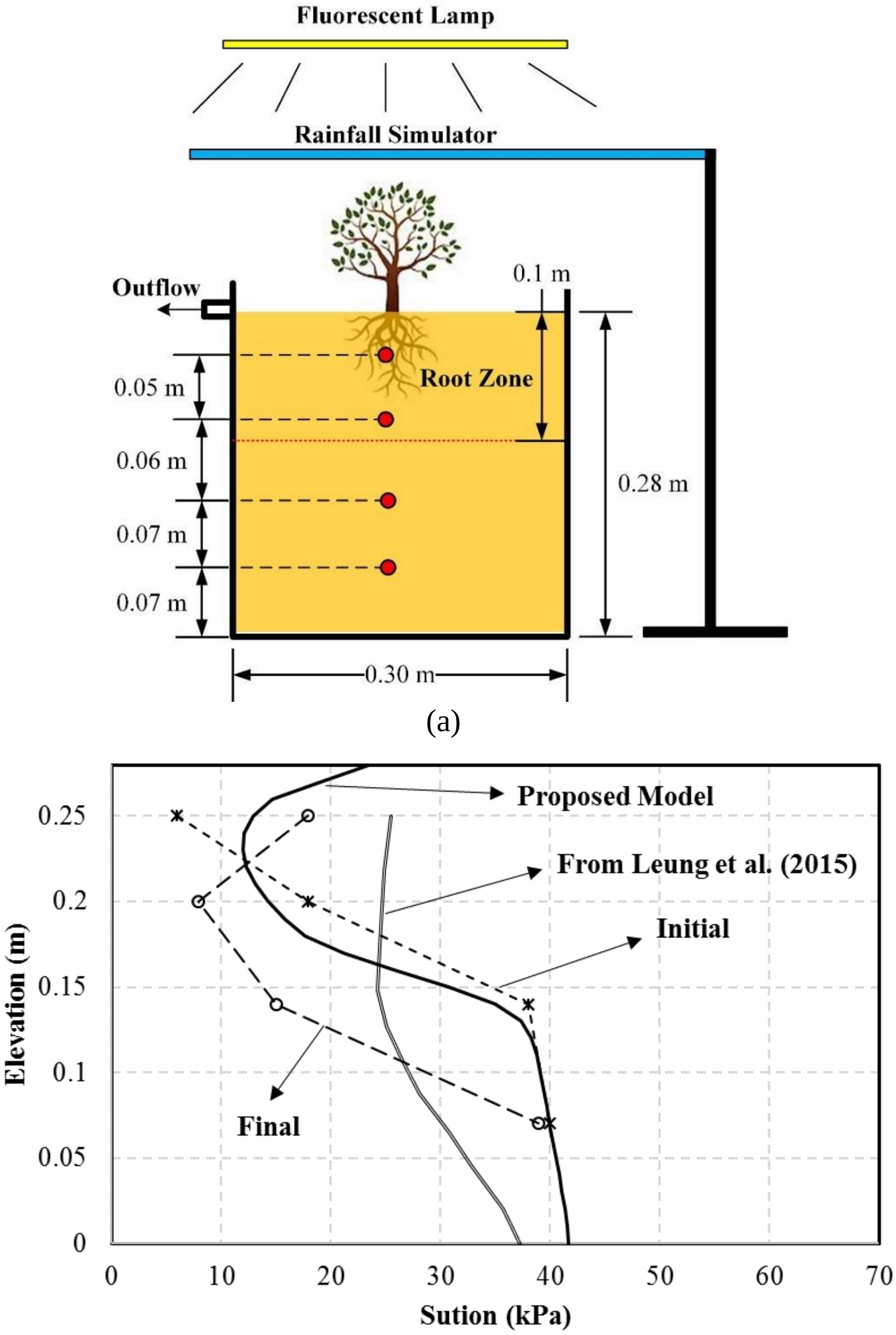

(a)

(b)

Figure 3 FEM model calibration. (a) schematic plot of test setup, and (b) comparisons of laboratory test and simulation results.

Chapter. 4 Model Configurations and Material Inputs

The model configuration is shown in Figure 4a. The flexible pavement is treated as a two-layered system subjected to static wheel load. To reduce the calculation cost, half of a two-lane road was simulated, and the road was 0.5 m-thick in the longitudinal direction. The pavement structure consists of a 0.1 m-thick Asphalt Concrete (AC) and a 1.0 m-thick base course. The slope ratio (vertical: horizontal) is 1:3, with grass hydroseeded on road slope. The grass root depth (H) is important in controlling the water exchange between the soil and the ambient environment and assumes to be 0.1 m-thick. An 80-kN (18-kip) single-axle load is often used as the standard vehicle or axle load in pavement designs and is assumed to be the case for this simulation. Each wheel included two tire loads (20 kN each) with a spacing of 0.34 m and the contact area assumed to be circular with a radius of 0.1 m. The pressure was uniformly distributed on top of the AC layer with a magnitude of 620 kPa. The groundwater table was assumed to be 0.5 m below the ground level. At the top of the base course, there was a 0.1 m thick water infiltration layer that was used to account for the precipitation infiltration. The water balance analysis of this layer was similar to that for the soil within the grass root zone, but with the ET term equals zero throughout the analysis (refer to Figure 2b). The difference between the infiltration layer and the underlying soil was that water balance analysis was only performed for the soil element within the infiltration layer. Since there was another AC surface course laid on top of the base course and no vegetation coverage on top of the base course at the driving lanes, the evaporation was set to be zero. As for the boundary conditions, the x-axis symmetrical boundary condition was applied at ① in Figure 4b. A fixed boundary condition was applied at ② and a roller boundary condition was applied at ③. The uniformly distributed wheel load was applied at ④. The displacement in z-axis was zero for all the nodes at the x-y plane. Zhang (2005) performed the analogue analysis between thermal-stress and consolidation problems and used the thermodynamic analysis in Abaqus software to simulate the consolidation theory for saturated-unsaturated soils. Due to the similarities between the coupled thermal-stress problem and coupled hydro-mechanical stress problem, the coupled thermal-stress analysis was performed. However, the pore water pressure in the hydro-mechanical analysis was analogue to the temperature in the thermal-stress analysis. Therefore, this study used a similar method, and the 8-node trilinear displacement and temperature element (C3D8T) was used in the analysis, as shown in Figure 4c.

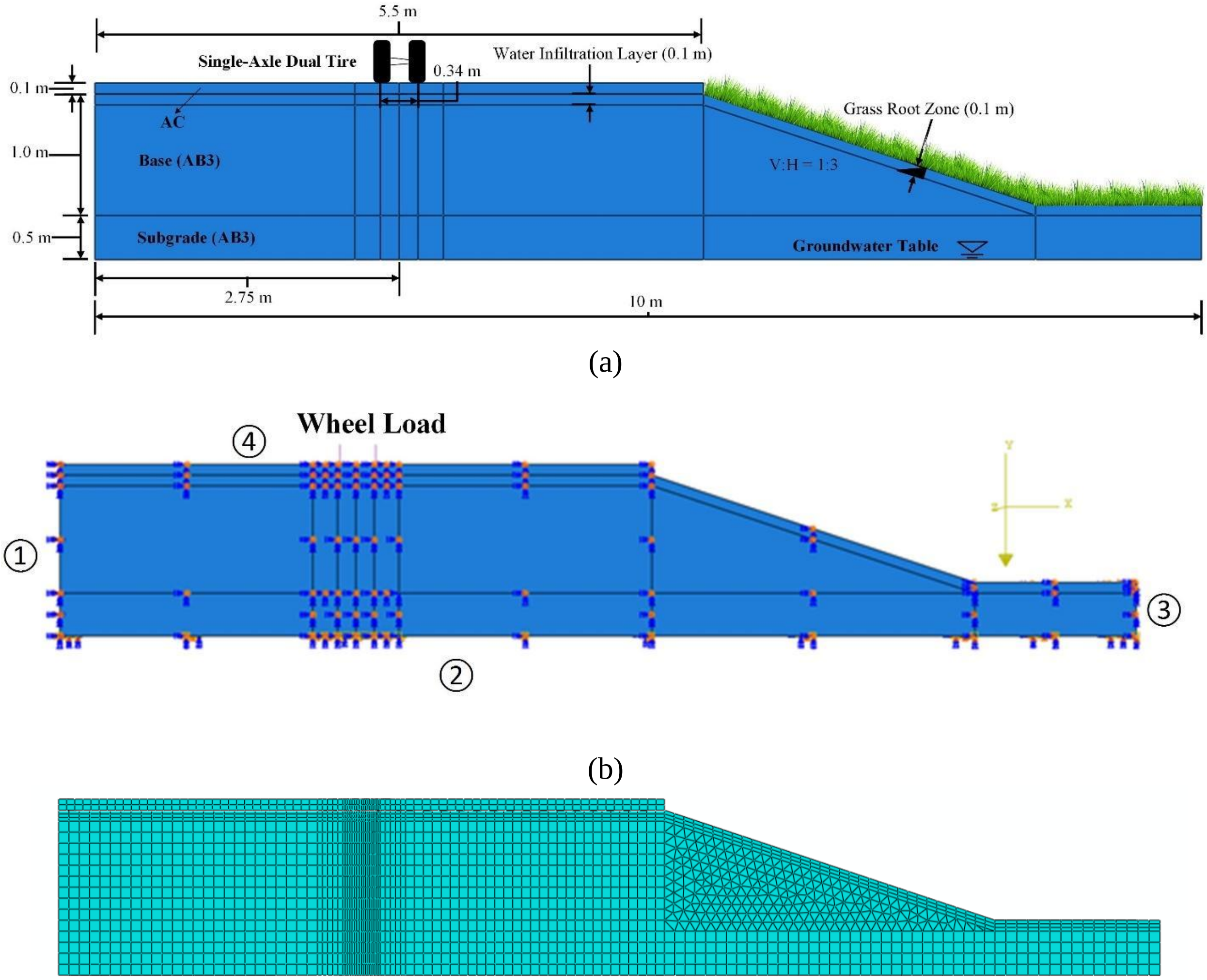

(a)

(b)

(c)

Figure 4 Model configurations. (a) geometry, (b) boundary conditions, and (c) mesh generation.

The material properties for the AC and base course are summarized in Table 1. Because this study focused on the resilient behavior of the base course, the properties of the AC layer assumed to be elastic with constant modulus and Poisson’s ratio of 1,000 MPa and 0.3, respectively. The AC layer was impermeable, and the effect of precipitation infiltration would be simulated via the water infiltration layer (refer to Figure 4a). To reduce the complexity of the numerical model, both the base course and subgrade assumed to be the same type of soil – Aggregate Base Class 3 (AB3) or well-graded gravel (GW-GC) according to Unified Soil Classification System (ASTM D24872011). Lin et al. (2018) performed a series of laboratory tests to characterize the hydraulic and mechanical properties of the AB3 and here only summarize the test results. The uniformity coefficient and coefficient of the gradation were 50 and 2.88, respectively. The AB3 contained about 10% of fines with Liquid Limit (LL) and

Plasticity Index (PI) of 20 and 7, respectively. The optimum water content for the AB3 was 8.5% based on the modified Proctor test and the corresponding maximum dry density was 2.1 Mg/m^3. The saturated permeability of the AB3 was 5.2×10^{-6} m/s and the saturation water content were 12.5%. As for the mechanical property of the base course, the resilient modulus test was performed according to AASHTO T309-99 (AASHTO 2003). The soil samples were tested at different water contents (ranged from dry condition (0%) to saturation condition (12.5%)). After the test, the universal model proposed by Uzan et al. (1992) was used (refer to Equation 9a) and modified to account for the influence of water content and stress state, as expressed in Equation 9b.

$$M_R = k_1 \times Pa\left(\theta / Pa\right)^{k_2} \times \left(\tau_{OCT} / Pa + 1\right)^{k_3} \text{ (Uzan et al. 1992)} \qquad (9a)$$

$$M_R = \left(30.448 - 2.854 \cdot wc\right) Pa\left(\theta / Pa\right)^{\left(-0.9174 + 0.2058 \cdot wc\right)} \times \left(\tau_{OCT} / Pa + 1\right)^{\left(0.854 - 0.5493 \cdot wc\right)} \qquad (9b)$$

where, k_1 to k_3 = regression parameters; M_R = resilient modulus, MPa; Pa = atmospheric pressure (i.e., 101 kPa); θ = bulk stress, $\sigma_1 + \sigma_2 + \sigma_3$, kPa; wc = water content, %; and τ_{OCT} = octahedral shear stress, $\tau_{OCT} = \frac{1}{3}\sqrt{\left(\sigma_1 - \sigma_2\right)^2 + \left(\sigma_2 - \sigma_3\right)^2 + \left(\sigma_1 - \sigma_3\right)^2}$, kPa.

For the hydraulic properties, the abilities of the AB3 to hold and transport water are two very important characteristics and can be represented by its soil water characteristic curve (SWCC) and its permeability function (also known as K-function). Detailed information about the testing procedures and test results for determining the SWCC and K-function could be found in another paper (Lin et al. 2018). The SWCC of the AB3 was determined via the pressure plate test and salt concentration test, and the regression curve can be expressed as in Equation 10. Since it was relatively difficult and time-consuming to laboratory determine the unsaturated hydraulic conductivity of a geomaterial, Kunze et al. (1962) proposed an indirect way of determining the unsaturated hydraulic conductivity function based upon the saturated conductivity and the SWCC. This method has been well accepted and became the state-of-art methodology. The K-function could be expressed as in Equation 11.

$$w = 12.50 \times C(\psi)\left\{1 / \ln\left[2.718 + \left(\psi / 2.35\right)^{1.241}\right]\right\}^{0.412} \qquad (10)$$

where, w = soil water content, %; $C(\psi) = 1 - \ln(1 + \psi / \psi_r) / \ln(1 + 10^6 / \psi_r)$; ψ = suction, kPa.; and ψ_r = residual suction, kPa.

$$k = 10^{\left(-0.0727 \cdot \log_{10}(\psi)^4 + 0.6053 \cdot \log_{10}(\psi)^3 - 1.7158 \cdot \log_{10}(\psi)^2 - 0.6322 \cdot \log_{10}(\psi) - 5.2956\right)} \tag{11}$$

where k = permeability of the AB3; and ψ = suction.

Table 1. Material Inputs of Pavement Layers

Material	Mechanical Properties		Hydraulic Properties	
	Modulus, *E* (MPa)	Poisson's Ratio,ν	SWCC	K-Function
AC	1,000	0.3	N/A	0 (impermeable)
AB3	Equation 9	0.35	Equation 10	Equation 11

In total two types of geotextiles were adopted in the numerical simulation. The mechanical and hydraulic properties are also listed in Table 2. The geotextile water characteristic curves (GWCCs) for the non-wicking geotextile (G1) and the wicking geotextile (G2) tested in the lab are expressed as in Equations 12 and 13 (Lin et al. 2019). Moreover, the mechanical interactions between the geotextile and the soil mass were determined via large-scale direct shear tests (Lin et al. 2018) and the corresponding interaction coefficient was 0.8.

$$w_{G1} = 50.60 \times C(\psi) \left\{ 1 / \ln\left[2.718 + \left(\psi/_{0.8} \right)^{2.062} \right] \right\}^{2.361} \tag{12}$$

$$w_{G1} = 33.0 \times C(\psi) \left\{ 1 / \ln\left[2.718 + \left(\psi/_{1.33} \right)^{2.947} \right] \right\}^{0.780} \text{ (if suction} \leq 50 \text{ kPa)}$$

$$w_{G1} = 5.19 \times C(\psi) \left\{ 1 / \ln\left[2.718 + \left(\psi/_{254.06} \right)^{1.732} \right] \right\}^{1.174} \text{ (if suction} > 50 \text{ kPa)} \tag{13}$$

where, w = water content, ψ = suction, $C(\psi) = 1 - \ln(1 + \psi / \psi_r) / \ln(1 + 10^6 / \psi_r)$, and ψ_r = residual suction, kPa.

The soil-geotextile interaction was depicted via the interface frictional angle. Lin et al. (2019) performed large-scale direct shear tests using granular aggregate and concluded that the interface frictional angle was not very sensitive to water content variations. In this numerical model, Mohr-Coulomb failure criterion was used, and the cohesion equaled to zero since the granular aggregate was used as the base course. According to the regression results from the laboratory tests, a constant interface frictional angle of 40º was assigned corresponding to the frictional angle at the designed optimum water content of 8.5% for the base coarse aggregate.

Table 2. Material Inputs of Geotextiles

Geotextiles [1]			
Property	Unit	G1	G2
		Mirafi RS580i (Reinforcement)	Mirafi H2Ri (Reinforcement + Drainage)
Wide Width Tensile Strength (MD/CD)	kN/m	7/26.3[2]	7/15.8[2]
AOS	mm	0.425	0.425
flow rate	$L/min/m^2$	3056	1222
permittivity	s^{-1}	1	0.4
GWCC[3]	-	Eq. 10	Eq. 11

Note:

[1] Values are provided by TenCate Mirafi specifications (TenCate, 2015, TenCate, 2005)

[2] Values are the ultimate tensile strength for G1, tensile strength @ 2% strain for G2 and G3

[3] Values are based on laboratory tests (Lin et al., 2019)

Chapter. 5 Base Course Resilient Modulus Variations with Time

To evaluate the seasonal variations of base course resilient behavior, three scenarios were simulated, representing different service conditions. Case I aimed at evaluating the performance of a new pavement, in which the pavement surface was in a good condition without any cracking. At this stage, the AC layer assumed to be impermeable and capillary action was expected to be the major detrimental factor influencing the pavement performance. For Case II, cracking was fully developed, and the pavement was moderately deteriorated with precipitation infiltrating into the pavement structure. The purpose of this simulation was to quantify the effect of different rainfall intensities and durations on the resilient behavior of a base course. Finally, Case III aimed at evaluating the seasonal variations in the resilient behavior of a base course for a moderately deteriorated pavement. The dynamic performance of the pavement structure and the interactions between the pavement structure and vegetation under localized climatic condition was assessed.

5.1 Case I: New Pavement without Cracking

Figure 5 shows the mean and shear stress distributions at different locations beneath the road surface. Three critical locations were selected: pavement centerline (center of the roadway), tire centerline (center of a single wheel), and axle centerline (center of the dual wheels). The bottom of the base course was selected to be a datum. At the pavement centerline, both mean and shear stresses linearly increased with depths under the influence of the overburden pressure. The wheel pressure had limited influence on the stress distributions at the pavement centerline due to a relatively long distance between the two locations. However, the mean stresses at both tire and axle centerlines first decreased under the influence of applied wheel load. As the wheel load influence decreased, the mean stress started to increase at an elevation of 0.8 m. The shear stress distribution at tire centerline decreased with elevation. However, the shear stress distribution at axle centerline first increased from 24.0 kPa (an elevation of 1.0 m) to 42.0 kPa (an elevation of 0.8 m), and then gradually decreased to 17.8 kPa at the bottom of the base course.

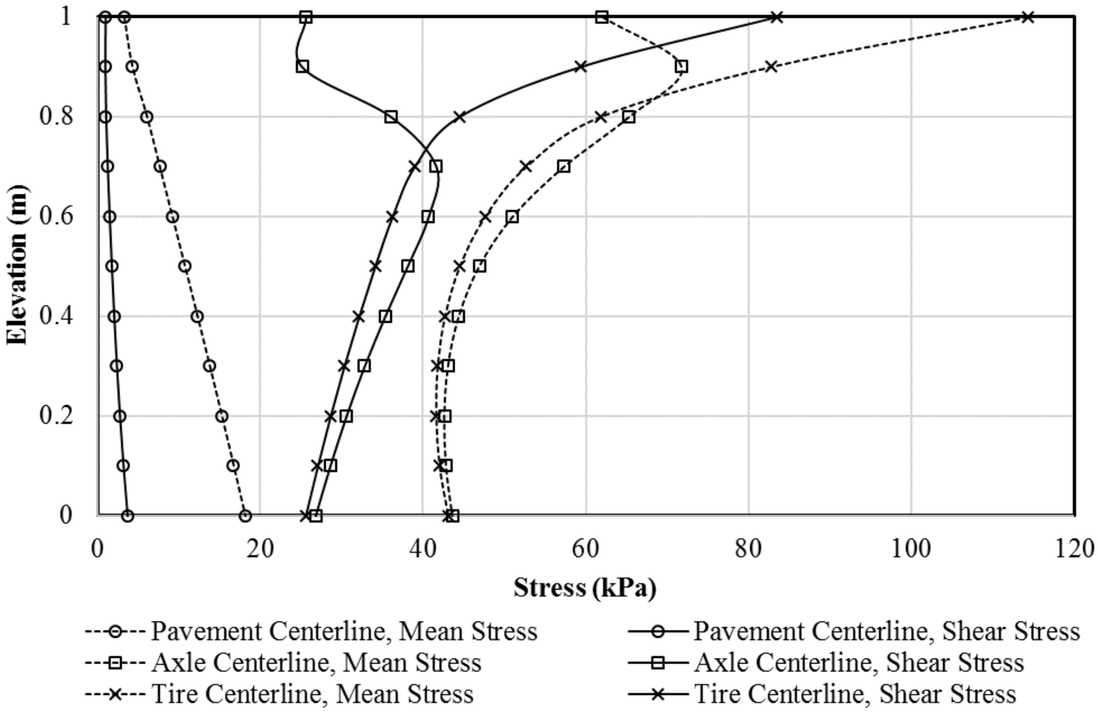

Figure 5 Stress distributions at different locations.

Figure 6 shows the suction, water content, and resilient modulus variations at three representative locations beneath the tire centerline: top, middle, and bottom of the base course. The base course was compacted at the optimum water content of 8.5%, corresponding to a suction value was 15.0 kPa and an average resilient modulus value of 262.0 MPa. These values will be considered as the references and will be used as the designed value for further discussions. In general, the water flow could be divided into two phases: free drainage and capillary action. For example, the soil suction at 1.0 m increased from 15.0 kPa to 18.5 kPa and the corresponding water content decreased from 8.5% to 8.2% within 7 days, as shown in Figure 6a. This phenomenon indicated that water was drained downward under the influence of gravitational force. In comparison, the soil suction value decreased from 18.5 kPa to 15.0 kPa on Day 52 and remained constant afterward. The capillary action was the major contributor to this suction decrement because the groundwater table was only 0.5 m below the datum. As for soils between 0.0 m and 0.5 m, the capillary action dominated the water flow process since suction values kept decreasing and the corresponding water contents continued to increase. At the equilibrium condition, the resilient modulus values (refer to Figure 6c) reduced by 30.6% at the top and 76.8% at the bottom of the base course, respectively. The simulation results indicated that even though the base course was designed to work under the optimum water content of 8.5%, the post-construction water content inevitably increased with time and the corresponding resilient modulus values were lower than the designed values. Therefore, the pavement deteriorations would be expected to occur earlier than expected under repetitive traffic load and the designed pavement service time would also be shorter than the designed value.

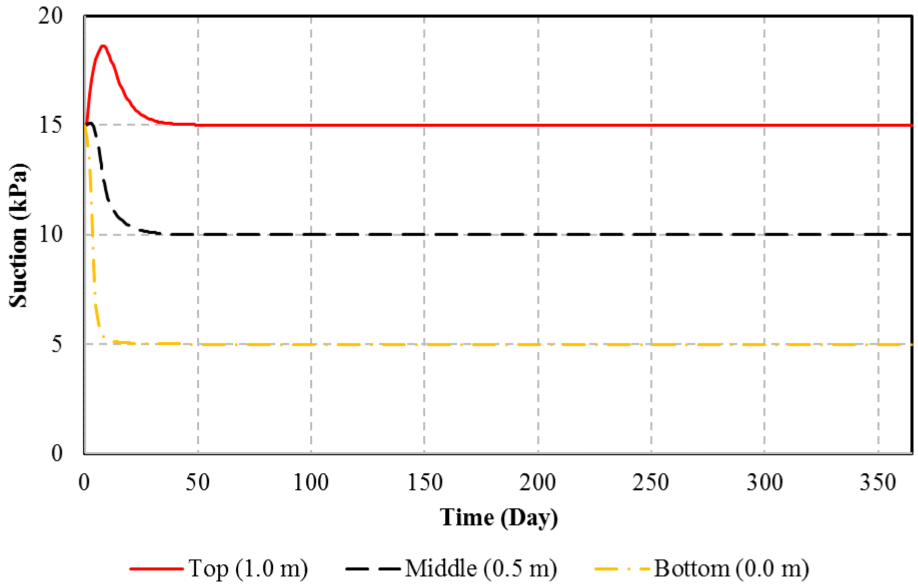

(a)

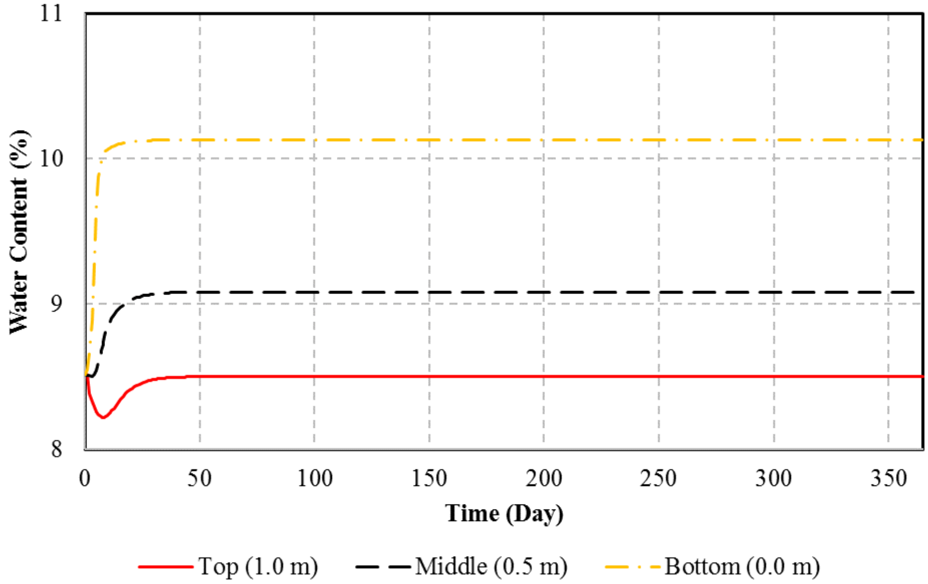

(b)

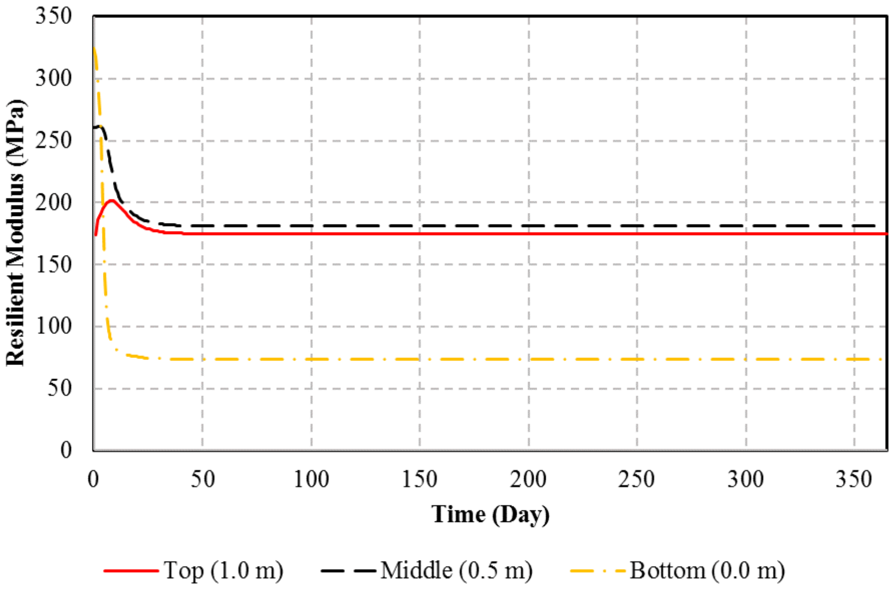

(c)

Figure 6 Simulation results for Case I (a new pavement without cracks). (a) suction variations with time, (b) water content variations with time, and (c) resilient modulus variations with time.

To better demonstrate the moisture migration within the base course, Figure 7 further presents the suction, water content, and resilient modulus distributions at the tire centerline at different times. At the steady-state condition, the suction distribution should be linearly distributed and could be expressed as in Equation 14 and in Figure 7a:

$$\psi = -\gamma_w z \tag{14}$$

where, ψ = suction; γ_w = unit weight of water; and z = elevation.

A suction of 15 kPa was the designed value, as shown in Figure 7a. From Day 1 to Day 7, the soil suction with elevations higher than 0.6 m increased due to the free drainage process. In comparison, from Day 7 to Day 52, the soil suction gradually decreased due to the capillary action and water migrated upward to the base course. Meanwhile, for soils with elevations lower than 0.6 m, the soil suction continuously decreased, indicating that only capillary action dominated the water flow in this section. In addition, the suction variations were significant from Day 1 to Day 30, indicating that the water flow was transient. From Day 30 to Day 52, the suction values slightly decreased until the steady-state was achieved on Day 52. All the suction values at the steady-state were lower than the designed values, indicating that the soil water content was higher than the designed value.

The water content variations with time were shown in Figure 7b. The designed water content was its optimum water content which equals to 8.5%. From Day 1 to Day 7, the water contents for soils higher than 0.6 m was lower than the designed value, indicating that the water flowed downward under the influence of gravity. Then, the water contents started to increase from Day 7 to Day 30 and remained relatively constant until the equilibrium state was obtained on Day 52. In addition, only the top 0.1 m soil meet the design value of 8.5%. This fact further proved the authors' assertion that no matter how well the pavement was constructed, the water content of the base course would inevitably increase with time due to the existence of the shallow groundwater table and capillary action.

Figure 7c further demonstrates the resilient modulus variations with time. Note that the resilient modulus of the base course was a function of soil water content, bulk stress, and shear stress. The designed values in Figure 7c were determined based upon the same designed water content of 8.5% but with different stress levels. From Day 1 to Day 7, the resilient modulus for soils higher than 0.6 m increased with time due to the decreasing water contents. However, the resilient modulus significantly decreased as the capillary water migrated upward to the base course. The lower the soil elevation, the closer the soil to the groundwater table and the lower the resilient modulus value would be expected. For example, the designed resilient modulus values for soil at 0.0 m was 324 MPa while this value decreased to about 73.5 MPa at the equilibrium condition, which reduced to about a quarter of the designed value.

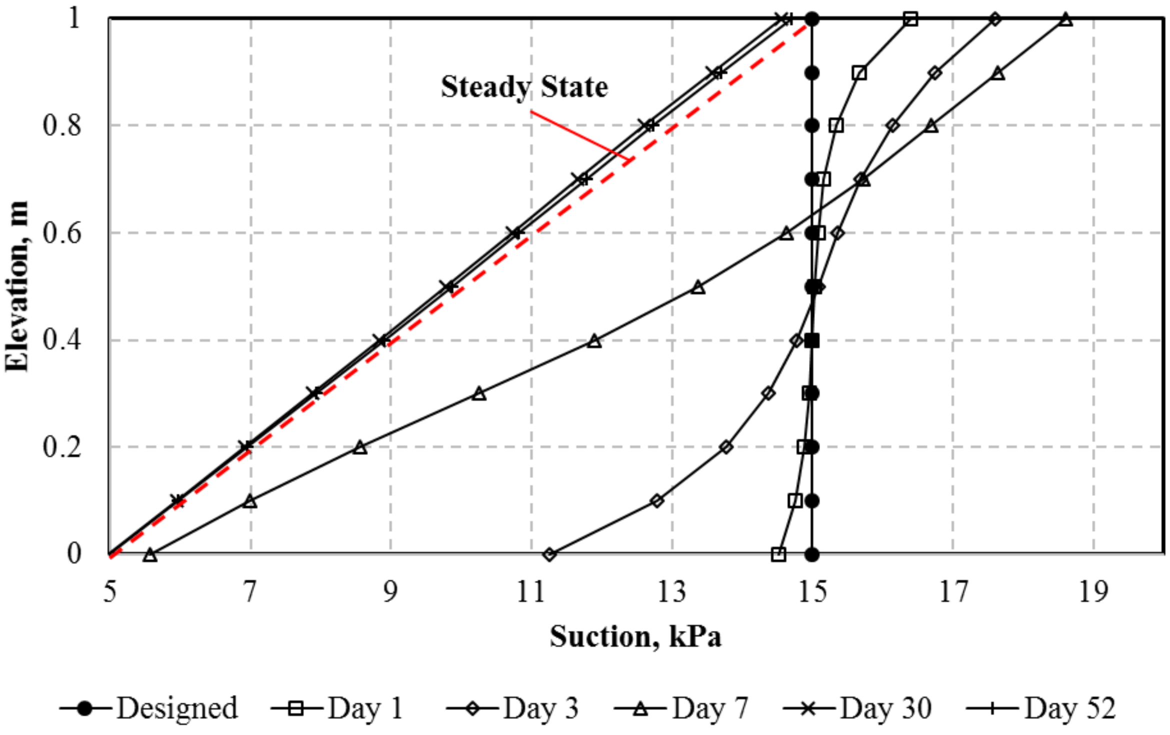
Steady State
Elevation, m
1
0.8
0.6
0.4
0.2
0
5
7
9
11
13
15
17
19
Suction, kPa
Designed
Day 1
Day 3
Day 7
Day 30
Day 52

(a)

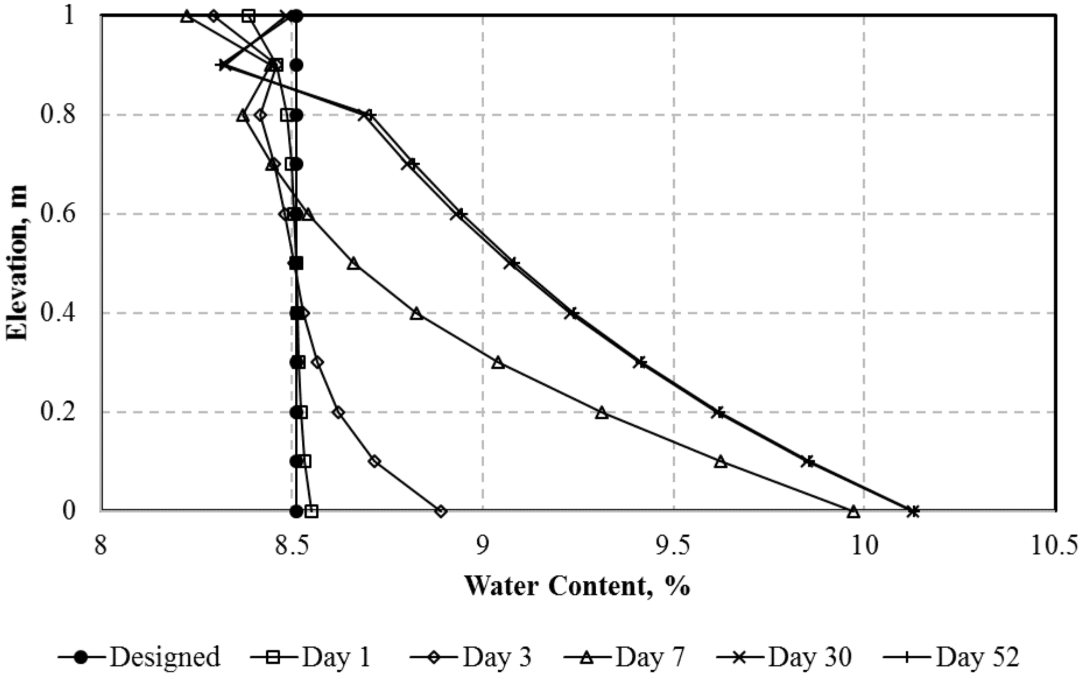
Elevation, m
1
0.8
0.6
0.4
0.2
0
8
8.5
9
9.5
10
10.5
Water Content, %
Designed
Day 1
Day 3
Day 7
Day 30
Day 52

(b)

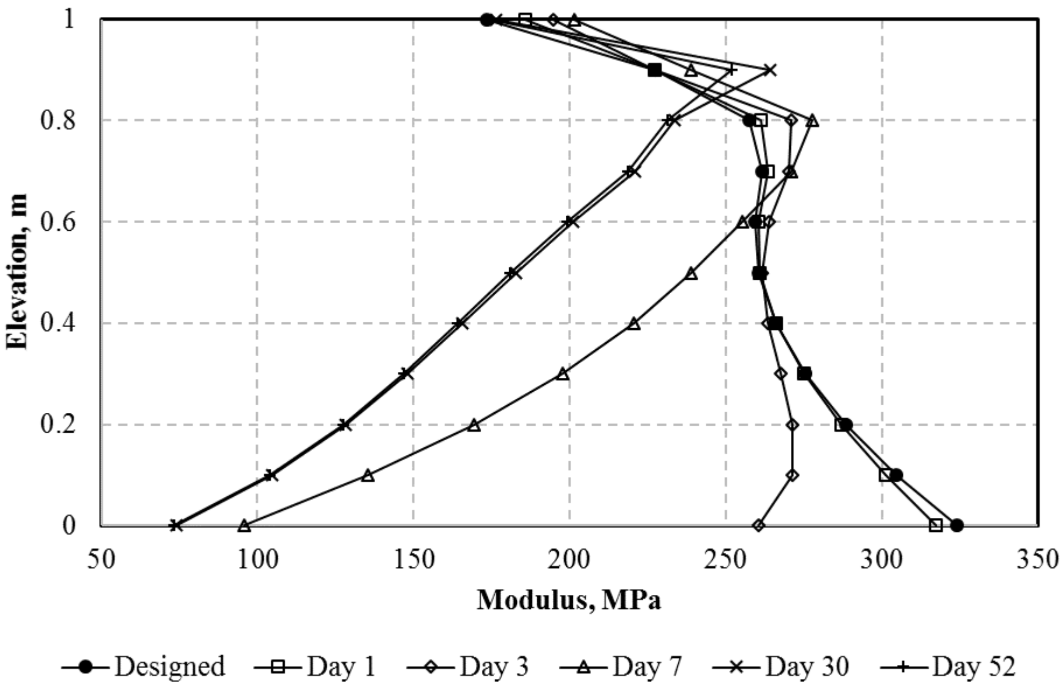

(c)

Figure 7 Suction, water content, and resilient modulus distributions at tire centerlines. (a) suction distributions at different times, (b) water content distributions at different times, and (c) resilient modulus distributions at different times.

In conclusion, the soil resilient modulus was very sensitive to soil water content variations. The average post-compaction water content of the base course would be higher than the designed value of 8.5%, and the corresponding resilient modulus would also be much lower than the designed value with a maximum reduction of 75%.

5.2 Case II: Moderately Deteriorated Pavement with Rainfall Events

Precipitation infiltration and capillary action are two major sources that result in pavement deteriorations (Elsayed and Lindly 1996; Huang 2004). Case I has evaluated the influence of the capillary action. The infiltration water would penetrate into the pavement structure via cracks and Van Sambeek (1989) reported that surface water infiltration could account for as much as 90% to 95% of total moisture in a pavement system. In practice, the infiltration rate cannot exceed a fraction of the precipitation rate and Ridgeway (1982) proposed Equation 15 to determine the infiltration rate. Case II aimed at evaluating the influence of rainfall intensity and duration on the resilient behavior of the base course and three scenarios were simulated. The total amount of cumulative infiltration water was the same for all three scenarios (0.12 m/day) but with different intensities and durations: (i) 0.005 m/h for 24 hours, (ii) 0.040 m/h for 6 hours, and (iii) 0.120 m/h for 1 hour. The time intervals between two rainfall events were 60 days so that the influence of the previous rainfall event would not influence the upcoming one.

$$q = 0.0305(N + 1 + \frac{W_p}{C_s}) \tag{15}$$

where, q = infiltration rate, m^3/h/linear m; N = number of traffic lanes; W_p = width of the pavement subjected to infiltration, m; C_s = spacing of transverse cracks, m.

Figure 15 shows the suction, water content, and resilient modulus variations with time at different locations beneath the tire centerline. The 1st rainfall event occurred on Day 60 when the pavement system already reached the equilibrium condition. As shown in Figure 15a, the entire base course was influenced by the 1st rainfall event as the soil suction at the bottom of the base course slightly decreased from 5.0 kPa to 4.7 kPa three days after the rainfall event. In addition, the suction variations for the top 0.4 m soil were more significant because the soil there was closer to the top of the base course where infiltration water came into the base course. Similar trends were also observed for the 2nd and 3rd rainfall events. However, it is important to point out that the influence of rainfall duration was much significant than the intensity. The reasons may be explained in two folds. Firstly, a longer rainfall duration required a longer time for the suction to recover to the same level. For example, the 1st rainfall event lasted for 24 hours and it took 30 days for the suction value to recover to the value before the rainfall event (15 kPa). However, this recovering time was only 20 days and 15 days for the 2nd and 3rd rainfall events, respectively. If the soil became saturated, the amount of water percolating to the underlying soil was constant and most of the water would be considered as runoff water. Therefore, the longer the rainfall lasted, the larger amount of water would infiltrate into the base course. Since the rainfall duration was 24 hours for the 1st rainfall event (the longest one), it also took the longest time for the soil to recover to the suction value before rainfall event. Secondly, longer rainfall events would result in higher magnitudes of suction changes. For instance, the maximum suction variation for the 1st rainfall event was observed at 1.0 m and the suction decreased by 8.8 kPa. In comparison, the maximum suction variations for the 2nd and 3rd rainfall events were observed at the same elevation but with lower magnitudes of 8.4 kPa and 5.4 kPa, respectively. In conclusion, rainfall events with longer durations would result in a higher magnitude of suction change and a longer recovering time to reach a steady-state again.

Similar observations were observed in the water content, as shown in Figure 15b. For the 1st rainfall event, the intensity was mild (5 mm/day) but lasted longer (24 hours). The soil at the top of the base course became wet (but not saturated) and its permeability significantly increased with the increasing soil water content. As long as the soil was not saturated, all the infiltration water could be absorbed by the water infiltration layer (refer to Figure 4a) and would percolate to the underlying soil. However, for the 2nd and 3rd rainfall events, the soil within the water infiltration layer was saturated and any additional water would be considered as runoff water and could not infiltrate into the pavement structure. This is why the water content variations in the middle were less significant in the 2nd and 3rd rainfall events than in the 1st one. In other words, the influence of the rainfall duration on soil resilient behavior was more important than the rainfall intensity.

Figure 15c further demonstrates the resilient modulus variations with time during the rainfall events. As mentioned in the ***Introduction*** section, the resilient modulus of a base course was determined via FWD test on a bi-weekly or monthly basis. However, those values only represented the resilient modulus at that period of the year (AASHTO 2008) and might not accurate enough to represent the monthly average value. For example, during the 1st rainfall event, the resilient modulus values decreased from 176 MPa to 59.3 MPa within one day and increased to 159 MPa after two weeks. Suppose the field engineer performed the FWD test one day after the rainfall stopped, the value of 59.3 MPa was obviously much lower than the monthly average value. Therefore, the resilient behavior of the base course was significantly influenced by the rainfall intensity and duration. The numerical simulation of the seasonal variations of the resilient modulus of the base course should be conducted using hourly climatic data so that the influence of precipitation infiltration could be reasonably reflected. In addition, the numerical simulation results can also provide guidance to the field engineers regarding the appropriate time to conduct a field test. For example, if the rainfall duration was relatively long (e.g. the first rainfall event), engineers should wait at least 2-3 days until the resilient modulus was recovered to at least 80% of the value before the rainfall event. However, if the duration of the rainfall was very short, most of the water would be runoff rather than infiltrate into the pavement structure and the field engineers could perform the test one day after the rainfall event. It is important to point out that the although EICM provides environmental data on an hourly basis, the analysis period (design life) was divided into 1-month or 2-weeks periods according to the MEPDG manual (ARA 2004). That is to say, the simulation of the resilient behavior based on the EICM model was accurate enough to capture the effect of rainfall intensity and duration on the resilient behavior of a base course while the proposed model has such capability.

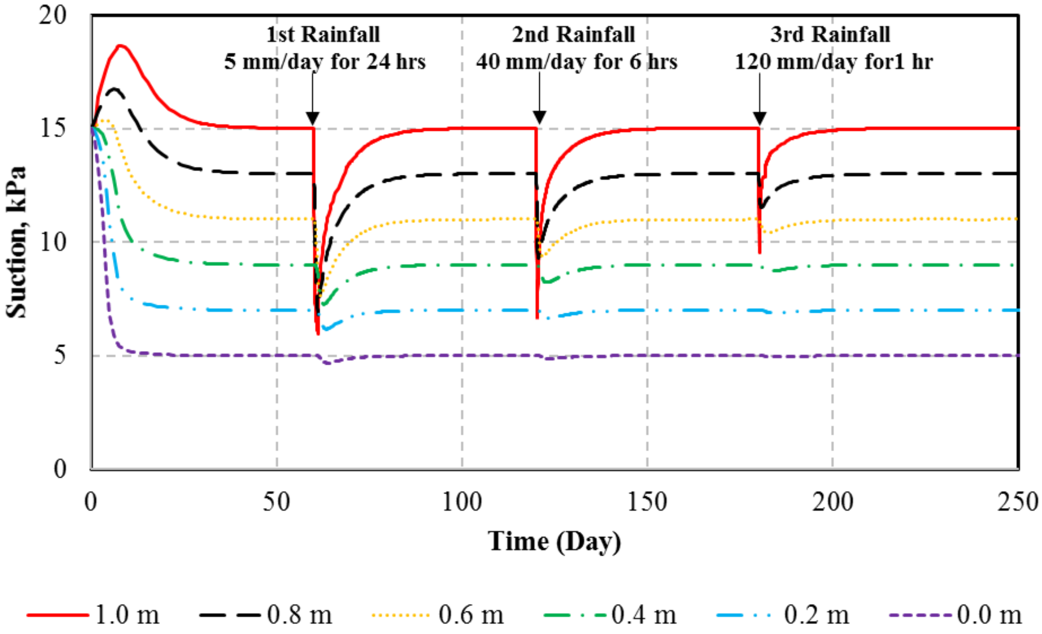

(a)

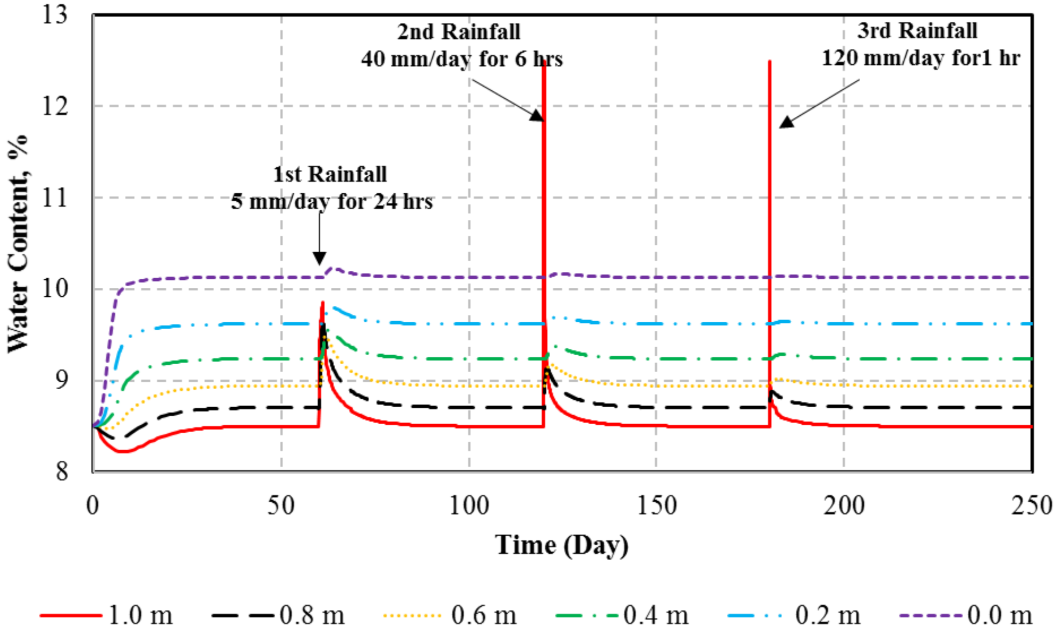

(b)

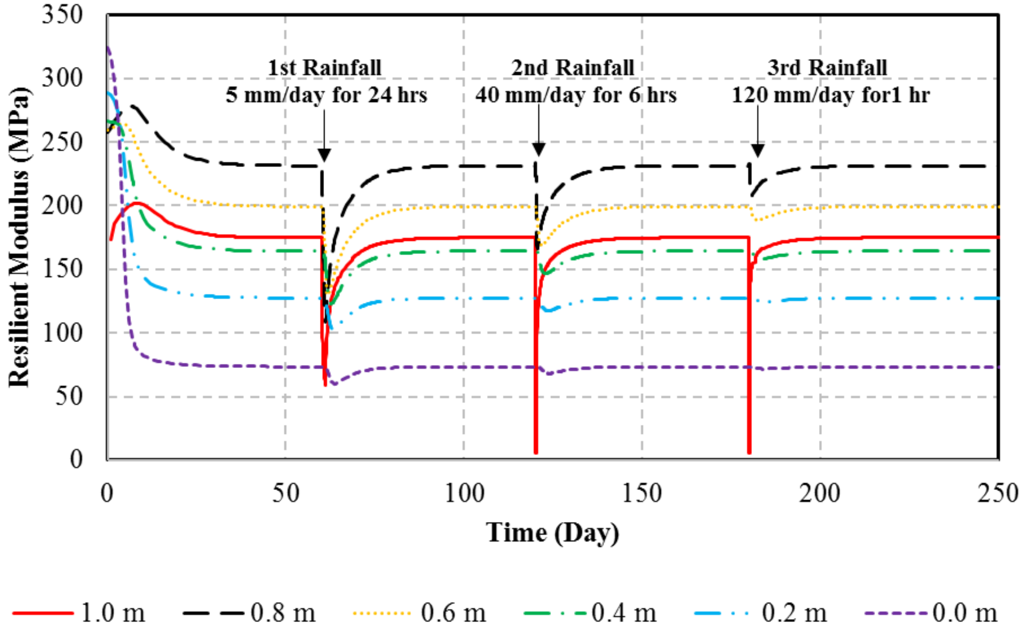

(c)

Figure 8 Simulation results for Case II (moderately deteriorated pavement with fully developed cracks). (a) suction variations with time, (b) water content variations with time, and (c) resilient modulus variations with time.

To further quantify the amount of infiltration water that entered into the pavement structure,

Figure 9 shows the amount of precipitation and runoff water during the rainfall event. The area between the two curves would be the total amount of infiltration water. As shown in Figure 9a, during the 1st rainfall event, even though the intensity of the rainfall was not significant (only 5 mm/hr), it lasted for 24 hours. There was no runoff water during the entire rainfall event and all the infiltration water went into the pavement structure (in total 0.12 m). In comparison, runoff water was observed during the 2nd rainfall event and the total amount of infiltration water was only 0.0498 m (Figure 8b), which account for 41.5% of the 1st rainfall event. It is important to emphasize again that the influence of rainfall duration was much significant than its intensity in affecting the resilient behavior of the base course. As the rainfall intensity continued to increase to 0.12 m/hour and its duration time continued to decrease to 1 hour (Figure 9c), there was even less amount of infiltration water. During the 3rd rainfall event, there was only 0.009 m of water infiltrated into the pavement structure, which was only 7.5% and 18.1% of that for the 1st and 2nd rainfall events. In comparison, the amount of infiltration water that enters into the top of the unbounded base course was not accurate in the EICM model. In the MEDPDG approach, the infiltration can assume four values – none, minor, moderate, and extreme (0%, 10%, 50%, and 100% of precipitation enters the pavement). However, based on the simulation results in this study, given the same amount of cumulative precipitation, the rainfall event with a longer duration would have much devastating influence on the soil resilient behavior because it allowed the base course to be exposed to the wet condition for a longer time. In other words, the proposed model is more accurate than the EICM model in predicting the resilient behavior of a base course.

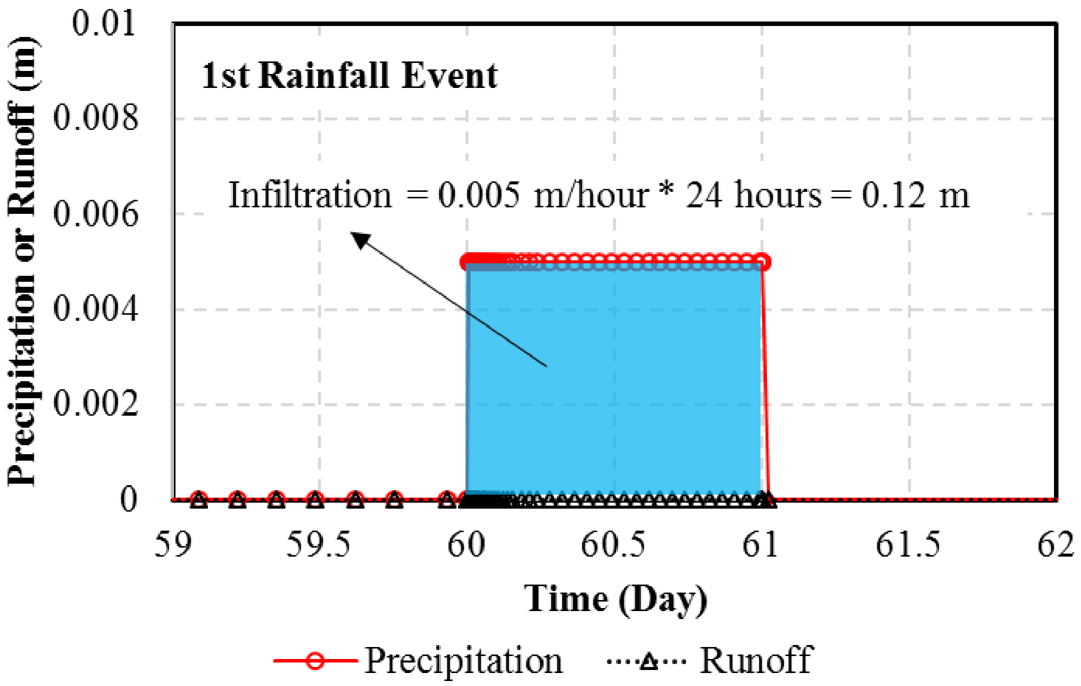
1st Rainfall Event
Infiltration = 0.005 m/hour * 24 hours = 0.12 m
Precipitation or Runoff (m)
0.01
0.008
0.006
0.004
0.002
0
59
59.5
60
60.5
61
61.5
62
Time (Day)
Precipitation
Runoff

(a)

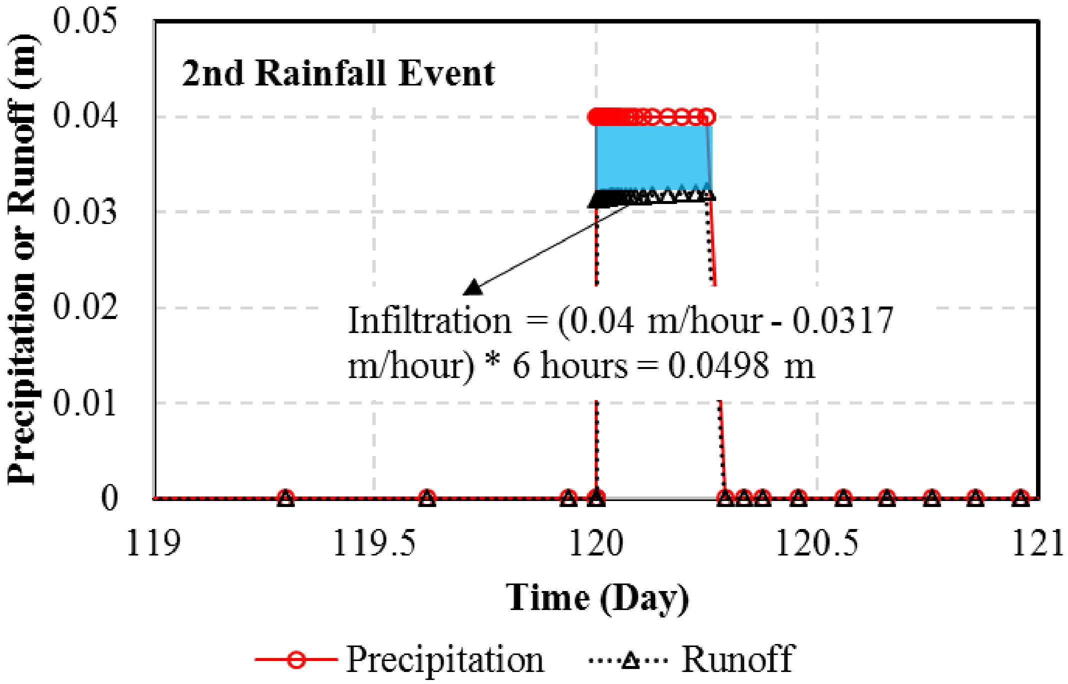
2nd Rainfall Event
Infiltration = (0.04 m/hour - 0.0317 m/hour) * 6 hours = 0.0498 m
Precipitation or Runoff (m)
0.05
0.04
0.03
0.02
0.01
0
119
119.5
120
120.5
121
Time (Day)
Precipitation
Runoff

(b)

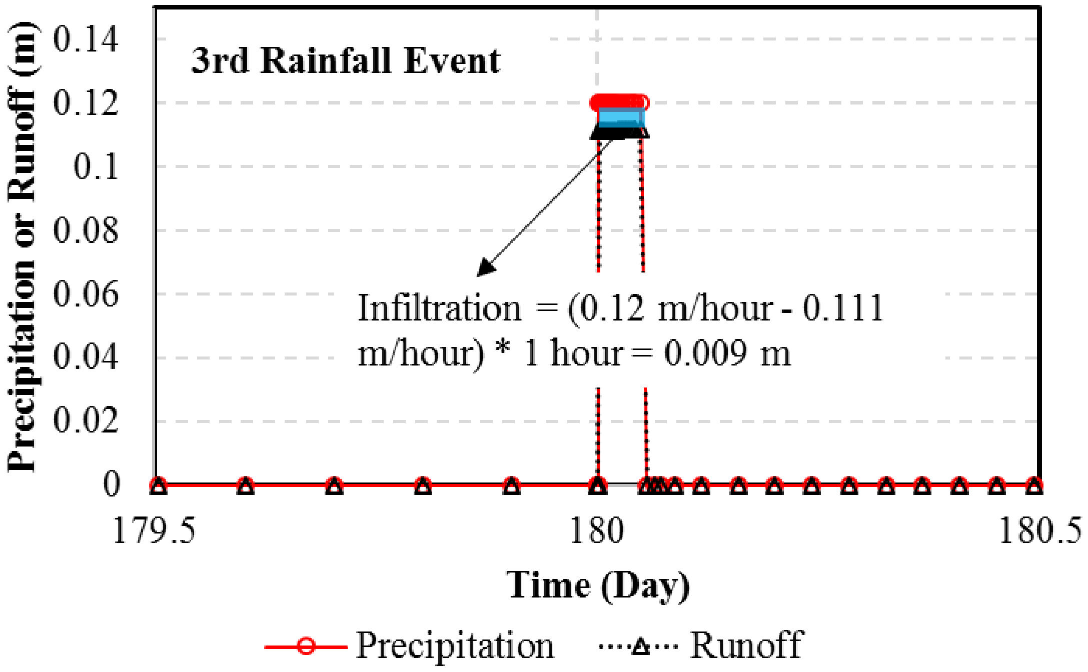

(c)

Figure 9 Comparisons of total amount of water infiltrated into the pavement structure. (a) 1st rainfall event (0.005 m/hr for 24 hrs), (b) 2nd rainfall event (0.040 m/hr for 6 hrs), and (c) 3rd rainfall events (0.120 m/hr for 1 hr).

Figure 10 shows the resilient modulus contours before and after each rainfall event. Four representative time frames were selected, including 1day before the rainfall event, right after, 1 day, and 7 days after the rainfall event. The blue (cold) color represents wet soil with low resilient modulus values while the red (warm) color represents dry soil with high resilient modulus values. As shown in Figure 10a, the soil resilient modulus was very high at the road slope with the highest value of 1300 MPa (upper left image). As the elevation of the soil on the road slope decreased, the soil suction was expected to decrease due to the existence of the shallow groundwater. A lower suction value corresponded to a higher soil water content and a lower resilient modulus. Then the rainfall event lasted for 24 hours and the precipitation water was allowed to infiltrate from both the grass root zone (road slope) and the water infiltration layer. As shown in the upper right image in Figure 10a, the maximum soil resilient modulus on the road slope significantly decreased from 1300 MPa to 520 MPa, reduced to approximately half of the value before the rainfall event. The resilient modulus value for the soil within the pavement structure even decreased from 175 MPa to 60.2 MPa, reduced to one-third of the value before the rainfall event. This observation indicated that the effect of infiltration water had a stronger influence on the pavement than on the road slope. After 1 day (the lower left image in Figure 10a), the soil at the top of the base course was still in wet condition. The relatively drier soil in the middle had lower permeability, impeding the excess water from percolating to the underlying soil. The resilient modulus contour 7 days after the rainfall event showed a similar trend as before the rainfall event.

Figure 10b shows the resilient modulus contours for the 2nd rainfall event. Because the time lag between the 1st and 2nd rainfall events was 60 days, the influence of the 1st rainfall event was negligible. Similar to the 1st rainfall event, the resilient modulus was much higher on the road slope than within the pavement structure (upper left image). However, due to the higher rainfall intensity, the soils at the top of the base course and on the road slope were saturated right after the rainfall event (upper right image). The saturated soil impeded additional precipitation water from infiltrating into the pavement structure, resulting in a relatively drier condition 1 day after the rainfall (lower left image) when compared with that for the 1st rainfall event. After 7 days, the soil resilient modulus contours recovered to the condition before the rainfall event. As for the 3rd rainfall event (Figure 10c), there was only 0.009 m of water infiltrated into the pavement structure. This fact explained why the resilient modulus values 1 day after the rainfall event was much higher in the 3rd rainfall event than those in the 1st and 2nd ones. Moreover, the EICM model is a 1D model that cannot be used to simulate the moisture migration in the transverse direction. In comparison, the simulation results in this study indicated that soil at the road slopes experienced a more significant water content variations compared with the soil in the middle of the road since the soil at the road slope was closely affected by the ambient environment.

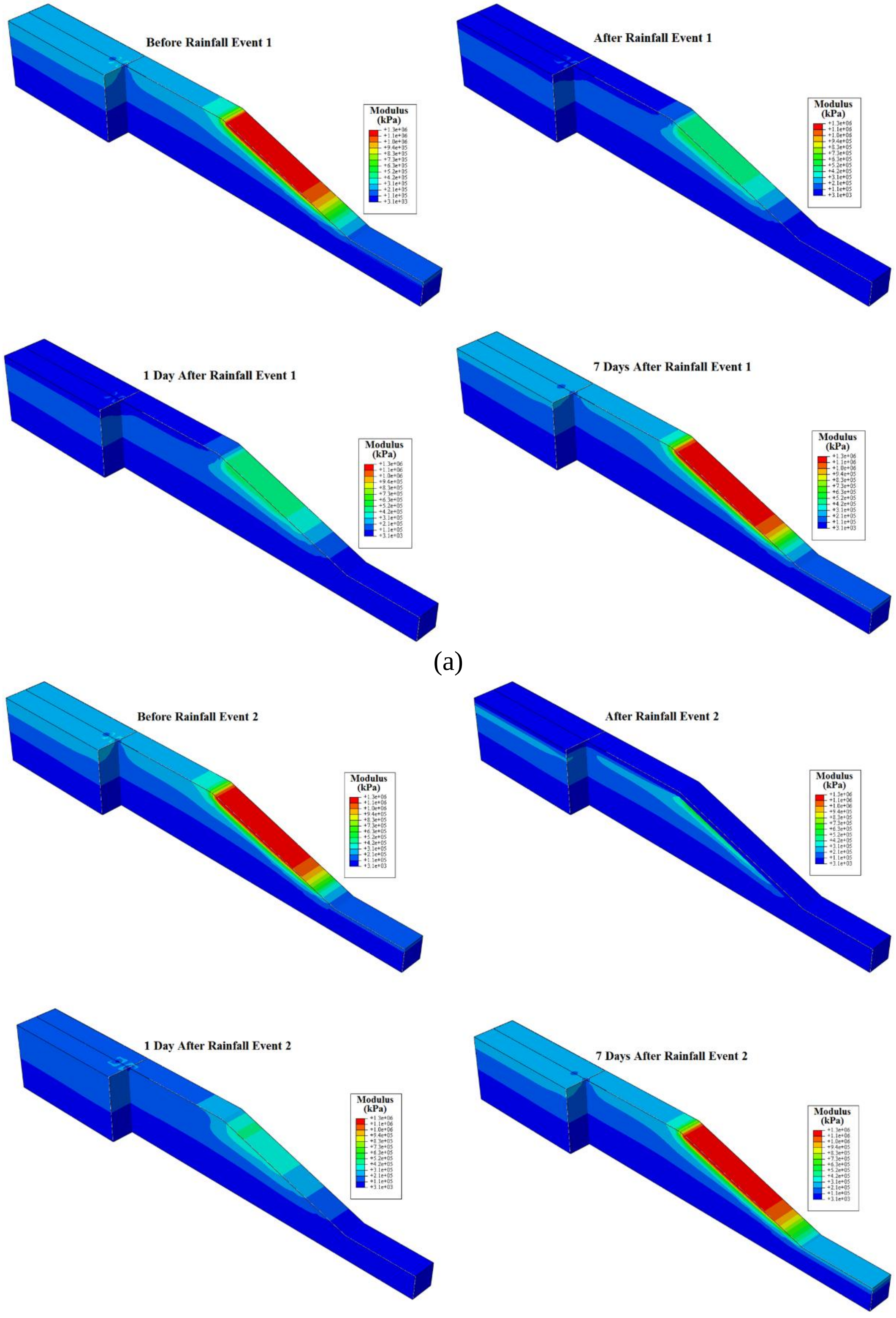
Before Rainfall Event 1
After Rainfall Event 1
1 Day After Rainfall Event 1
7 Days After Rainfall Event 1
Before Rainfall Event 2
After Rainfall Event 2
1 Day After Rainfall Event 2
7 Days After Rainfall Event 2
Modulus
(kPa)
+1.3e+06
+1.1e+06
+1.0e+06
+9.4e+05
+8.3e+05
+7.3e+05
+6.3e+05
+5.2e+05
+4.2e+05
+3.1e+05
+2.1e+05
+1.1e+05
+3.1e+03

(a)

(b)

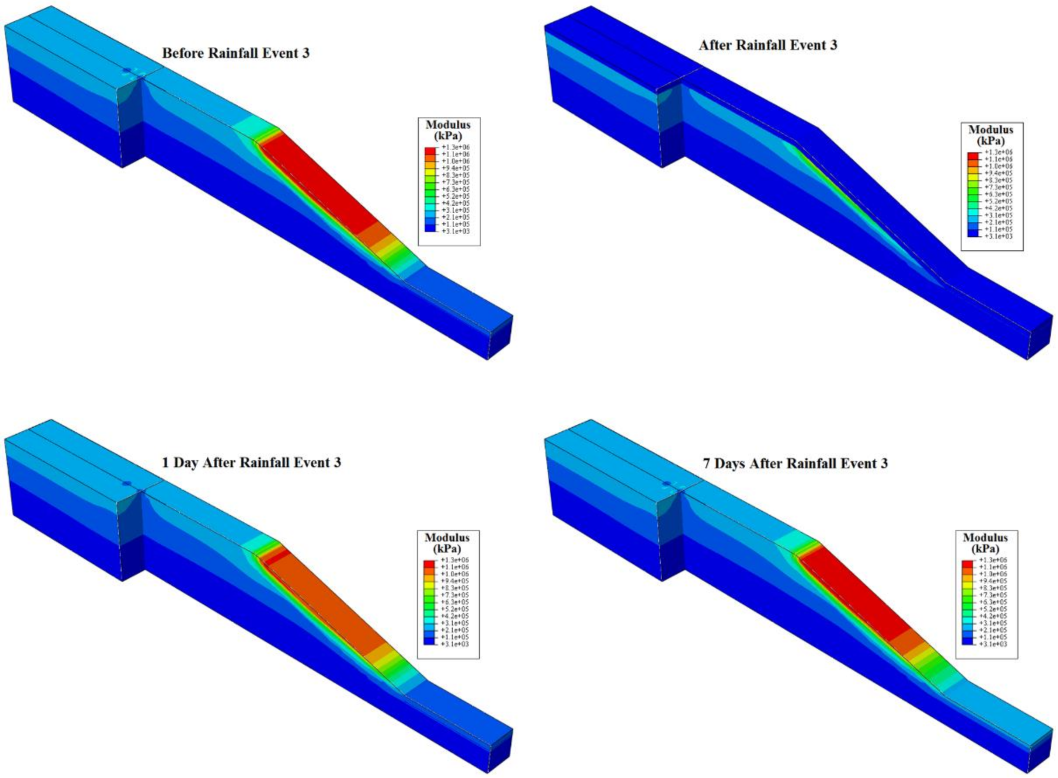

(c)

Figure 10 Resilient modulus contours during rainfall events. (a) 1st rainfall event, (b) 2nd rainfall event, and (c) 3rd rainfall event.

In summary, the resilient behavior of the base course was sensitive to water content variations. With the same amount of cumulative precipitation, the rainfall event with a longer duration would cause the most significant resilient modulus reduction. The rainfall duration played a more significant role than the rainfall intensity in influencing the base course resilient behavior (without considering other influencing factors such as soil hydraulic conductivity and degree of saturation).

5.3 Case III: Pavement with Cracks and Real-Time Climatic Data

To reveal the dynamic base course resilient behavior under the influence of localized climatic condition, hourly meteorological data presented in Figure 1d was applied to the model. Cedergren (1974) proposed Equation 16 to correlate the infiltration rate with rainfall rate, and recommended a constant parameter, *C*, to be 0.33 to 0.5 for flexible pavement. In this report, the C value of 0.5, was used in this report, representing the scenario of a pavement structure with fully developing cracking.

$$q = CR \tag{16}$$

where, q = infiltration rate; C = fraction of infiltration that enters into pavement, equals to 0.5; and R = rainfall rate.

Figures 11a-c show the suction, water content, and resilient modulus variations with time. The significant drops in each figure indicated that there was a rainfall event occurred on that day. For example, the recorded precipitation on Day 10 was 2.54 mm, and the suction and water content changes during that day were 9 kPa and 0.9%, respectively. However, the amplitude of variation not necessarily reflected the rainfall intensity because soil field capacity also played a critical role in determining the amount of water infiltrating into the pavement structure. For instance, heavy rainfall was observed on Day 246 (with precipitation of 117.6 mm). However, the suction and water content variations were only 1 kPa and 0.15%, which were much smaller than those on Day 10. If the soil water content was higher than the field capacity, most of the precipitation water would be considered as runoff water. The difference between in-situ soil water content and soil field capacity depicts the water storage capacity. The soil water contents at Day 10 and 246 were 8.27% and 8.7%, indicating that the water storage capacity for Day 10 was higher than that for Day 246. In conclusion, the water content variation within the base course was a combined effect of precipitation and soil field capacity.

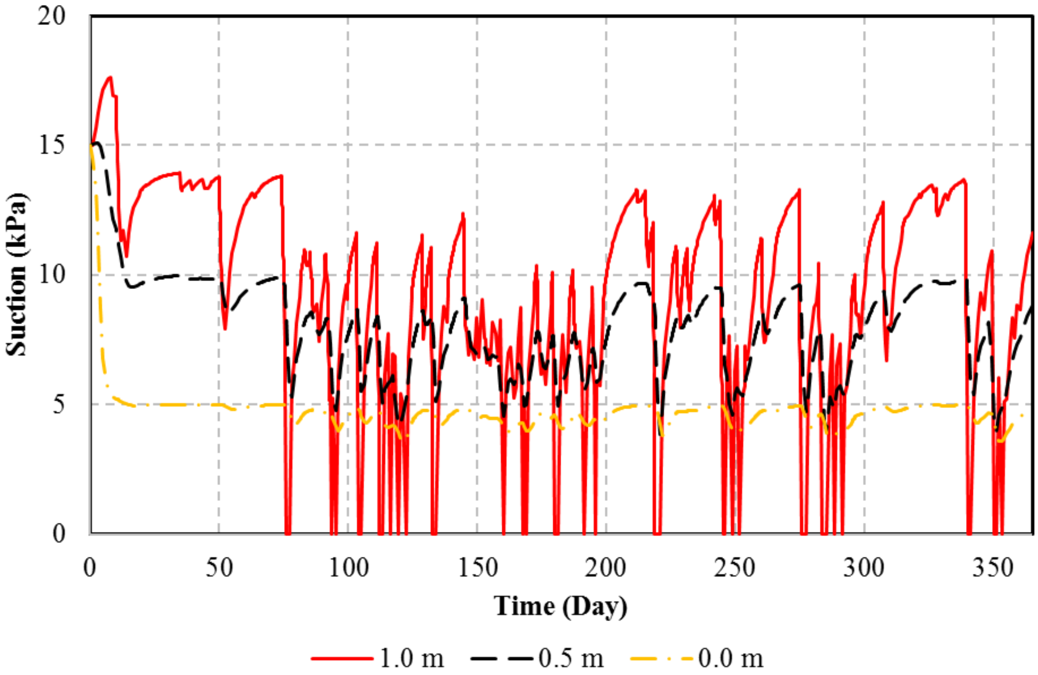

(a)

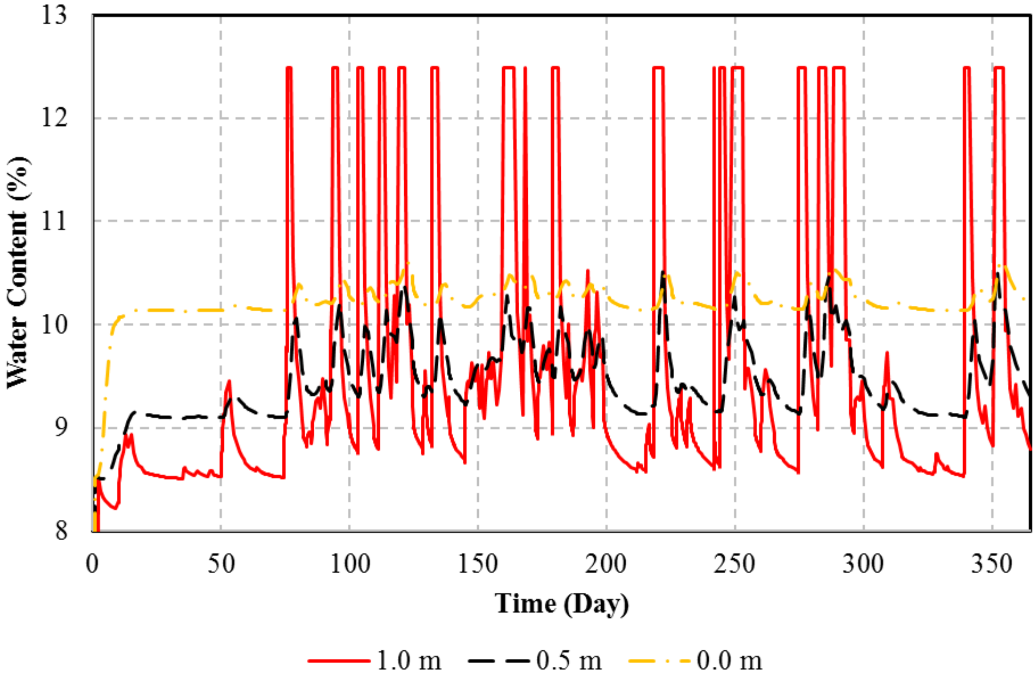

(b)

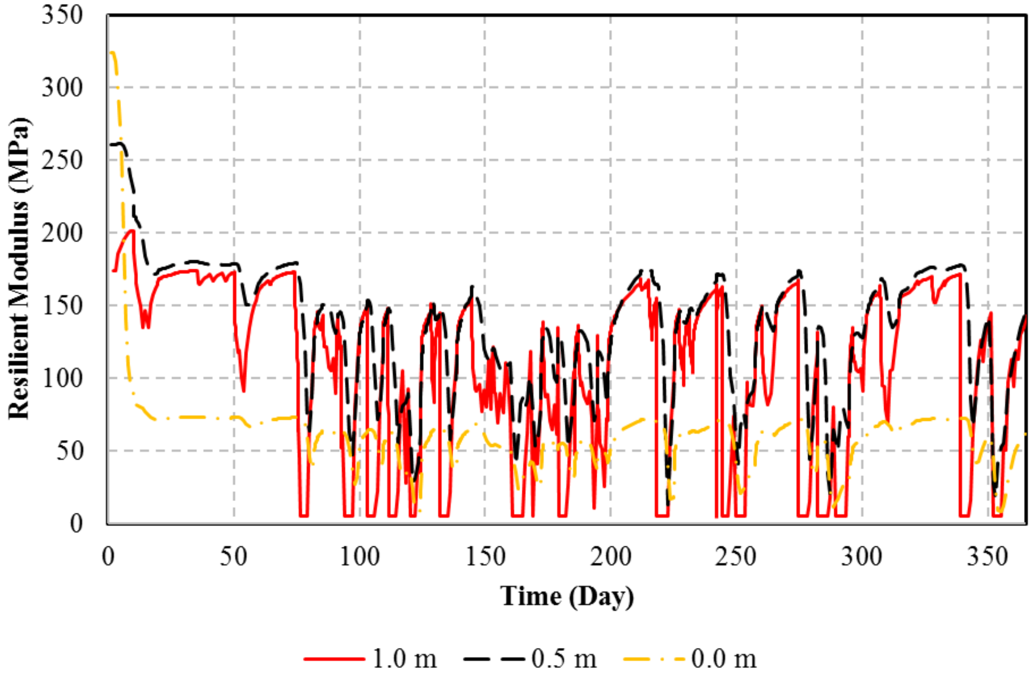

(c)

Figure 11 Simulation results for Case III (moderately deteriorated pavement with real-time meteorological data). (a) suction variations with time, (b) water content variations with time, and (c) resilient modulus variations with time.

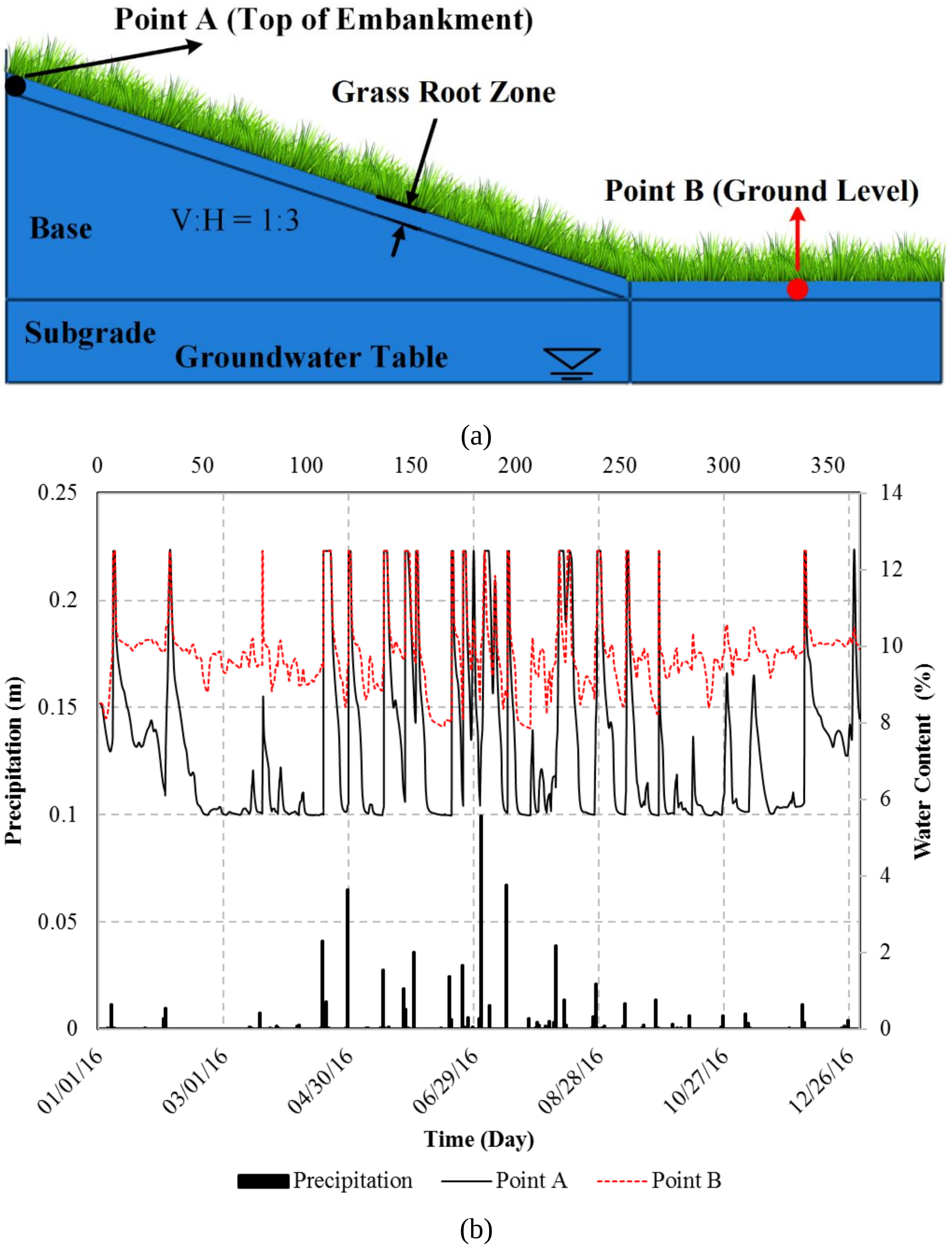

Figure 12 Water content variations with time at selected vegetation areas. (a) selected locations, and (b) water content variations.

Chapter. 6 Comparisons of Performance for Wicking and Non-wicking Geotextiles

In this section, three cases were simulated, including the control case (Case I), a pavement installed with the non-wicking geotextile for reinforcing purpose (Case II), and a pavement installed with the wicking geotextile (Case III). It is necessary to point out that the water table was assumed to be 1.0 m below the ground level, which was relatively shallow. In addition, the field test section was selected to be at Camdenton, Missouri, where continuous and heavy rainfalls were expected in the summertime. Detailed discussions regarding the simulation results are presented as follows.

6.1 Water Content Variations with Time

Figure 13a shows the water content variations with time beneath the wheel for the control case. The ground level was selected as the datum and the selected locations were at the bottom, middle, and top of the base course with elevations of 0.0 m, 0.2 m, and 0.4 m, respectively. As indicated in Figure 13a, even if the designed optimum moisture content for the base course aggregate was 8.5%, the actual water contents within the base course increased with time and were all above the designed value. In general, the water content was higher at the bottom of the base course due to a closer distance to the water table. In addition, significant water content fluctuations were observed throughout the entire base course, especially when heavy rainfall events were observed. For example, the water content increased from 9.3% to 10.1% at the bottom of the base course during the 68 cm rainfall event observed on Day 134.

Figure 13b further shows the water content variations for all three cases at the bottom of the base course. Firstly, the water content fluctuations were higher for pavement installed with geotextiles (either G1 or G2). The significant fluctuation was caused by the capillary break effect, as demonstrated by Zornberg et al. (2010). Capillary break effect was observed when two dissimilar geomaterials were in contact under unsaturated conditions. Since the pore sizes within the geotextiles were larger than those within the adjacent soils, the geotextiles tended to have a higher surface tension that trapped water in the voids rather than flowed downward. Consequently, as more water was trapped within the soil-geotextile interface, excess water accumulated at the soil-geotextile interface, as observed in Figure 13b. Secondly, the soil water contents reached the saturation value (12.5%) for Cases II and III. When the soil was saturated, positive pore water pressure was built up under a heavy axle load as discussed later and would result in a pumping issue. However, due to the high lateral drainage ability of G2, the duration of the saturation condition was much shorter for Case III (with G2, wicking geotextile) than Case II (G1, with the non-wicking geotextile).

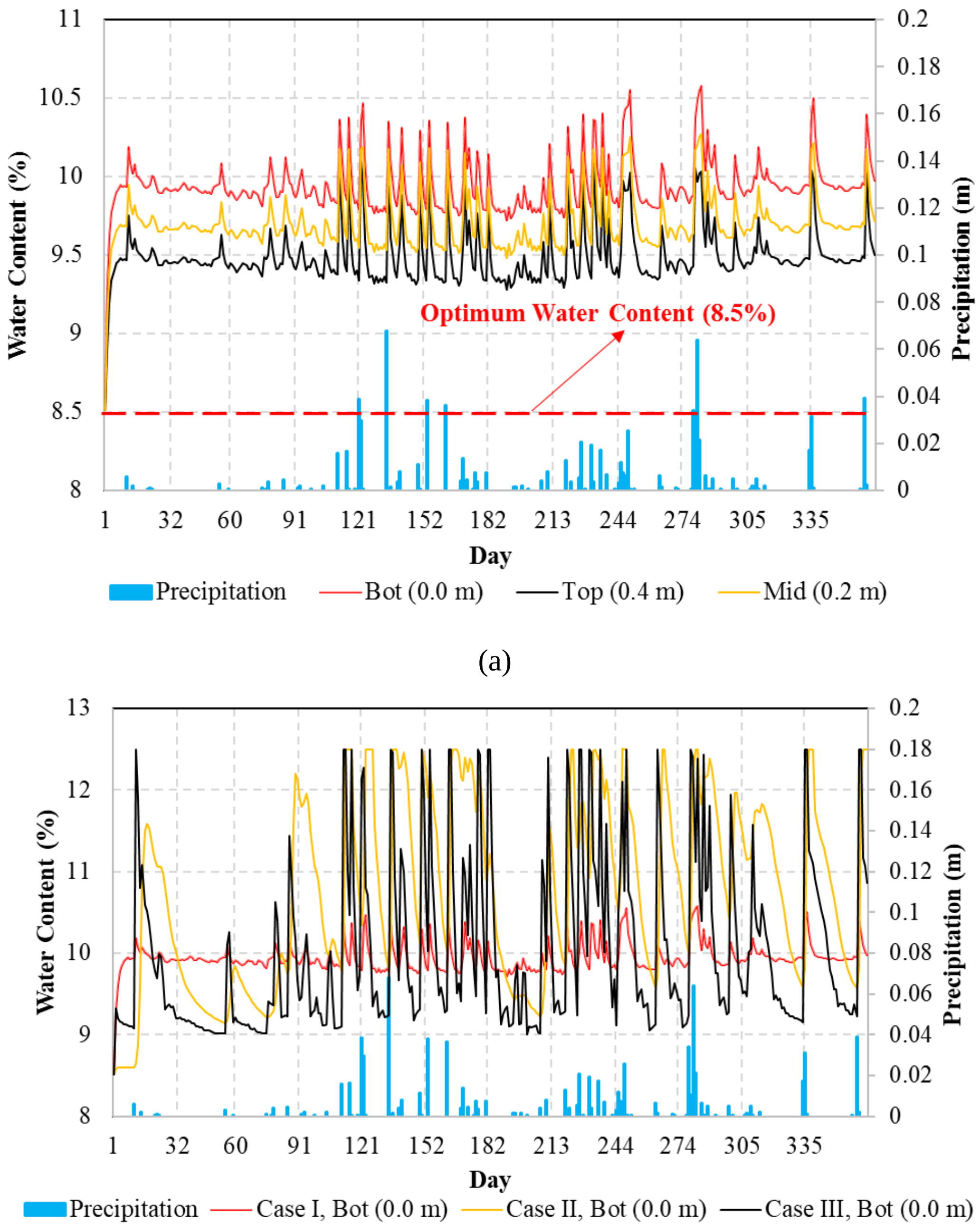

(a)

(b)

Figure 13 Water content variations with time. (a) different locations beneath the wheel load (Case I), and (b) at the soil-geotextile interface.

6.2 Resilient Modulus Variations with Time

Since the resilient behavior of the base course was a function of stress state and soil water content. Lin et al. (2019) pointed out that the soil sample would fail before conducting the test if the soil water content was higher than 10.8%. However, due to the existence of the shallow water table, the soil water content was expected to surpass 10.8%. The in-situ soil might survive because of the confinement provided by the adjacent soil but the exact resilient behavior could not be characterized in the laboratory. To avoid extrapolating the resilient behavior of the base course, the soil resilient modulus was assigned to be a constant number of 35 MPa (obtained in the laboratory resilient modulus test at 10.8% water content) when the soil water content was higher than 10.8%.

Figure 14a shows the resilient modulus variations with time for Case I. The base course was designed to work at the optimum water content of 8.5%, and the corresponding resilient modulus was 258 MPa. However, Figure 4a shows a significant reduction in resilient modulus within the first 12 days. The significant reduction was caused by capillary action. Secondly, the base course contained 10% of fines and was sensitive to water content variations. Even though the soil was first compacted at the optimum water content of 8.5% (refer to Figure 13a), the soil moisture content continued to increase due to the shallow water table. The average soil resilient modulus on Day 12 was about 93 MPa, which was only 36% of the designed value. The simulation results were consistent with those of other researchers (Abu-Fasakh et al. 2015). The soil water content inevitably increased with time due to capillary action, resulting in the resilient modulus much lower than the designed value.

Figure 14b shows the comparisons of resilient modulus variations at the bottom of the base course for three cases. The resilient modulus for Case I, which was the control case, was used as a reference to demonstrate the performance of the geotextiles. Within the first 70 days, the average resilient modulus value was 202 MPa in Case III, which was over 3 times higher than that in Case I, indicating that the wicking geotextile was effective in lateral draining water out of the pavement system. However, during the summer times when continuous and heavy rainfalls were expected, the soil resilient modulus values for Cases II and III were much lower than Case I. Because the precipitation data was on a daily basis, the rainfall duration was artificially elongated, resulting in excess water flowing back to the pavement system and significantly reducing the stiffness of the base course. The occurrence of this phenomenon was expected to be limited in the field as observed both in the laboratory tests and field tests (Lin et al. 2017; Lin and Zhang 2018b). On one hand, the precipitation data was based on a daily basis, which significantly underestimated the drainage efficiency of the wicking geotextile. On the other hand, when applied in the field, the wicking geotextile sheets often had an overlapping area, which impeded the water from flowing back to the base course.

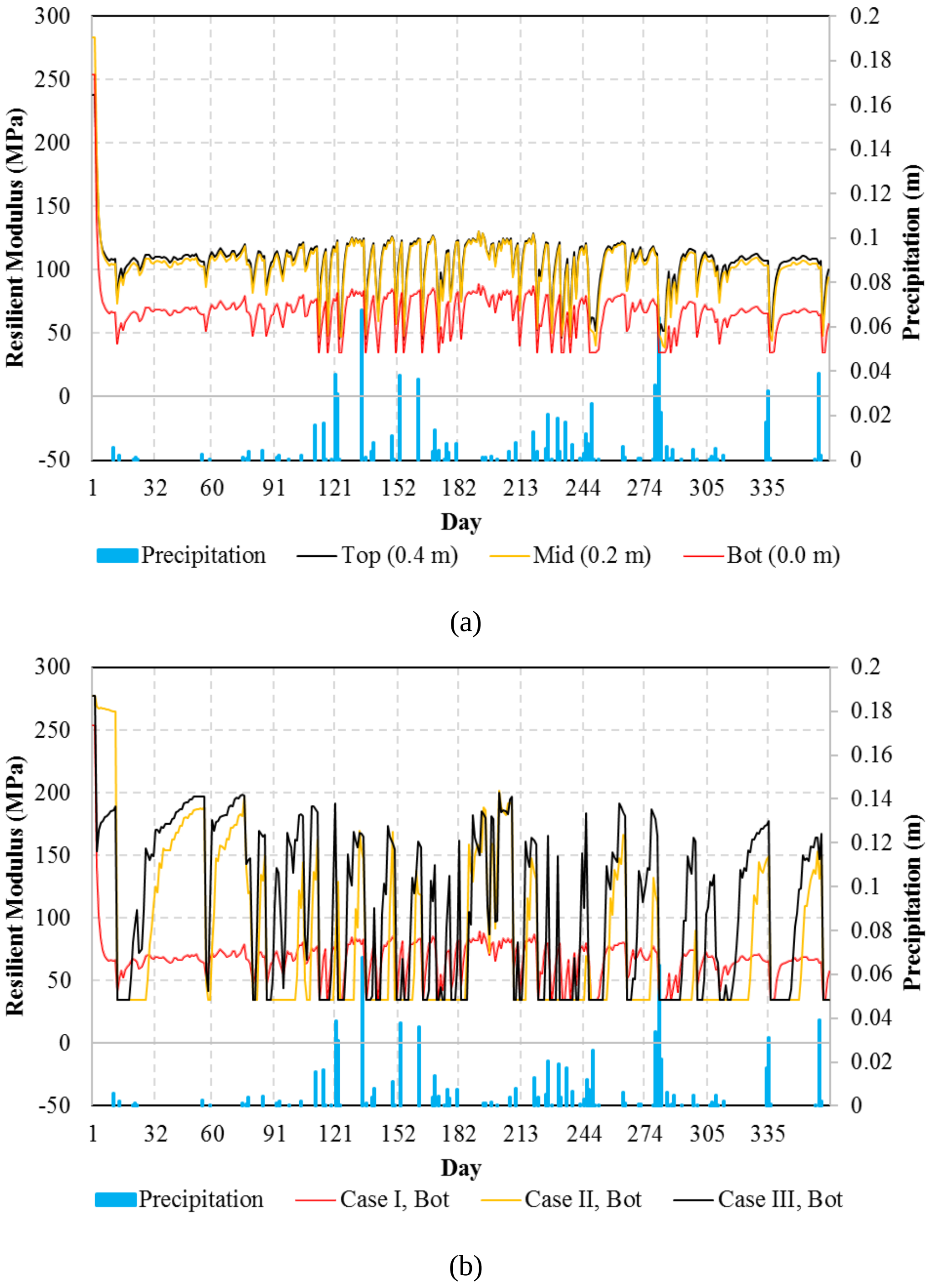

Figure 14 Resilient modulus variations with time. (a) different locations beneath the wheel load (Case I), and (b) at critical points (bottom of the base course) for different cases.

6.3 Pore Water Pressure Variations during Rainfall Events

Pumping is a common type of pavement distress causing a reduction in pavement life (Kermani et al., 2019). In general, three major factors contributing to the occurrence of pumping, including positive pore water pressure, high axle load, and high fine contents in the base course/subgrade layers. When the base course was saturated, the positive pore water pressure caused by the traffic load would force the fines in the base/subgrade to be exerted out to the road surface. Figure 8a shows the pore water pressure variations with time for Cases II and III at the soil-geotextile interface where the capillary break effect was expected to happen. The negative values of pore water pressure were also denoted as soil suction and meant that the soil was under unsaturated conditions. In other words, if the pore water pressure was positive, pumping might occur. The soil water content variation depended on rainfall duration, rainfall intensity, and current soil water content. In general, the soil would reach saturation when the precipitation was higher than the critical value of 13 mm. To further compare the drainage performance of the wicking geotextile, Figure 8b shows the pore pressure variations at the soil-geotextile interface for Cases II and III during a continuous rainfall event that was observed from Day 334 to Day 336. Due to the lack of hourly precipitation data, the following discussion was on a daily basis. The rainfall intensities were 17 mm, 31 mm, and 1 mm from Days 334, 335, and 336, respectively. Since both the rainfall intensity was higher than the critical precipitation (13 mm), the pore water pressure increased from negative to positive, indicating the soils for both Cases II and III changed from unsaturated to saturated. However, the pore water pressure for Case III decreased to -2.2 kPa on Day 336 when the rainfall stopped. In comparison, the pore water pressure for Case II remained positive for additional 3 days before the value became negative, indicating the soil became unsaturated. The simulation results indicated that G2 had a superior ability compared with G1 in terms of lateral draining water out of the pavement system.

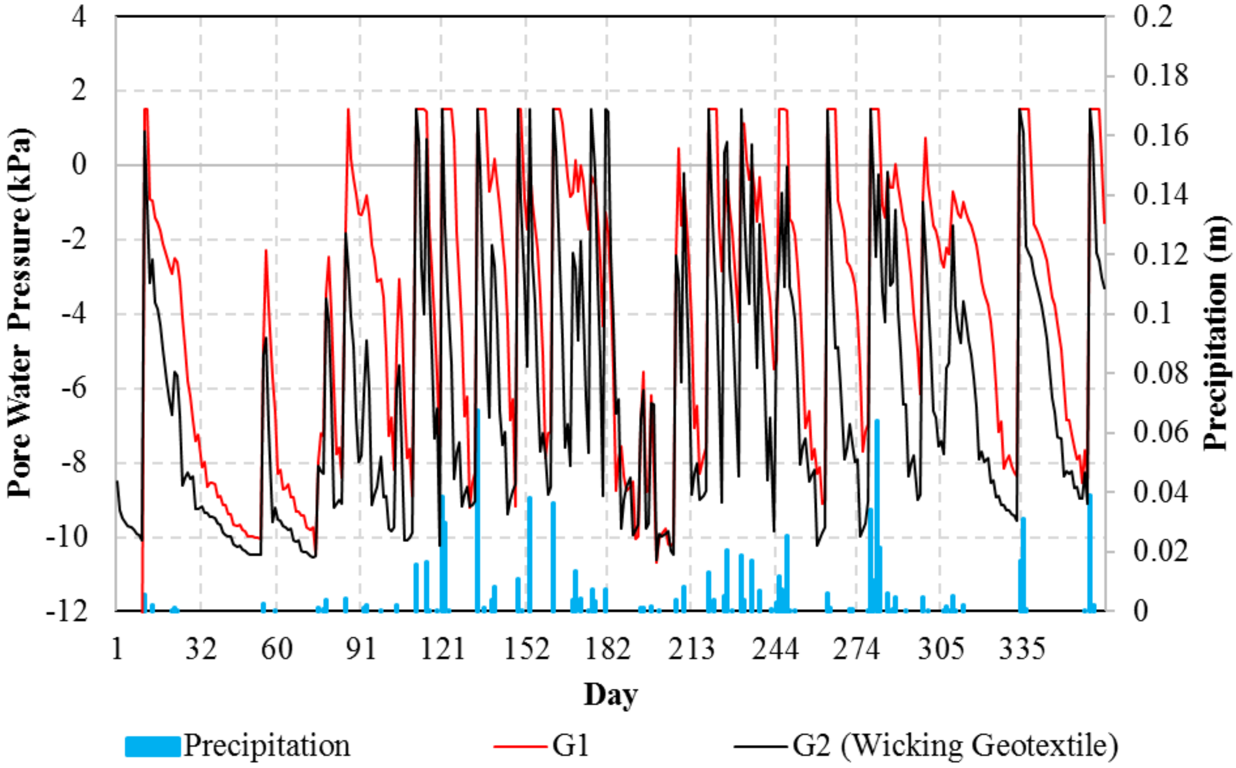

(a)

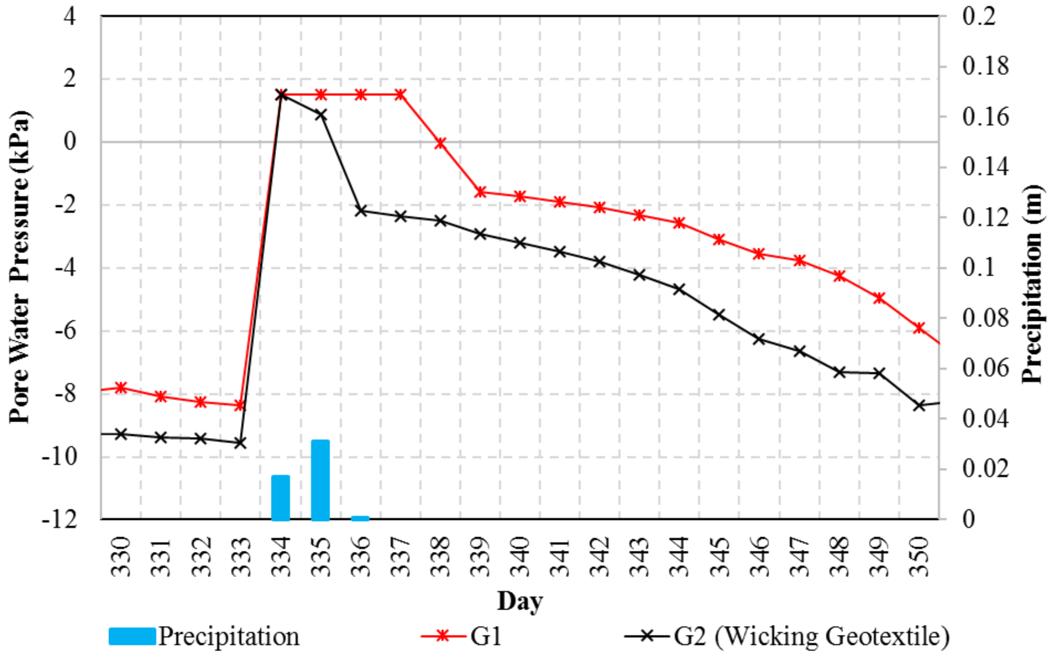

(b)

Figure 15 Pore water pressure comparisons. (a) Case II and Case III and (b) during a continuous rainfall event.

Figures 16a-b show the water content contours of the base course for Cases II and III before, during, and after the rainfall event observed on Days 334-336. As shown in Figure 16a, the highest and lowest water contents for Case II (with the non-wicking geotextile) were observed at the left bottom (10.0%) and the road slopes (8.5%), respectively. On Day 336 when the rainfall stopped, the water content on the right side of the road was 12.0%, approaching saturation. One day after the rainfall stopped, the soil was saturated and the bottom 0.15 m of the base course might cause pumping under repetitive traffic load. On Day 342, 6 days after the rainfall stopped, no saturation zone was observed within the base course. However, the water content was still at a very high level (near 12.0%) at the soil-geotextile interface. The simulation results indicated that the non-wicking geotextile did not have the ability to laterally drain water out of the pavement structure. In comparison, Figure 16b shows the water content contours of the base course for Case III during the same continuous rainfall events. It was important to point out that the water content for the top half of the base course was 8.5%, indicating that G2 worked more effectively than G1 in dehydrating the road embankment. Meanwhile, right after the rainfall stopped, the saturation zone was observed at the right half of the road embankment and was closer to the installation location of the wicking geotextile. This phenomenon proved the authors' argument that the wicking geotextile had a stronger lateral drainage ability. However, as mentioned before, this lateral drainage ability did not necessarily indicate the excess water would flow back to the embankment in the field condition. One day after the rainfall stopped, no saturation zone was observed and the highest water content was at the soil-geotextile interface and decreased from 12.5% to less than 11.0%. On day 342, three-quarters of the base course experienced a significant water content reduction and the water content was lower than 10.0%. In summary, the base course in Case III showed much better drainage performance than Case II and the wicking geotextile was more efficient in dehydrating the road embankment.

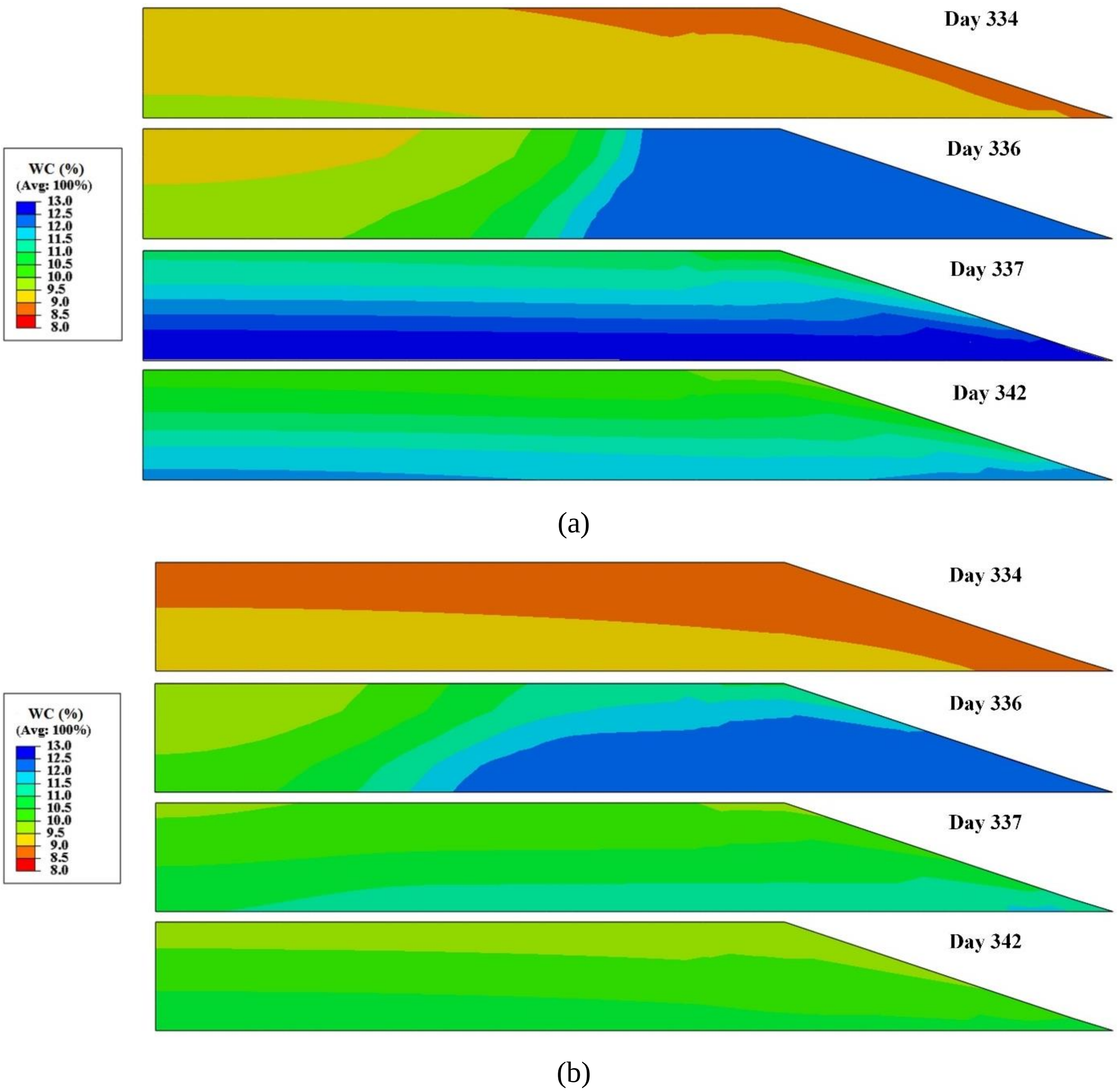

Figure 16 Water content contours: (a) Case II and (b) Case III

Chapter. 7 Incorporation of Wicking Geotextile Effects into Pavement Designs

The resilient modulus of a base course aggregate, M_R, is a measure of the stiffness and is considered as a critical material property input for pavement designs in both the AASHTO 1993 and the MEPDG design guides (Murad et al. 2015). Guo (2019) and Guo et al. (2019) firstly proposed the methodology to incorporate the benefits of the wicking geotextile into the pavement designs. However, the proposed methods were based on a rough estimation of “major rainfall” that could fully saturate the base course. The time period between two adjacent major rainfalls was defined as a drying period and the water content of the base course gradually decreased with time. Unfortunately, an accurate prediction of the daily water content variation of the soil aggregate was not available for the proposed method. Therefore, an accurate prediction of the resilient modulus variations was not feasible. In comparison, the proposed numerical model in this paper can accurately predict the seasonal variations of the resilient behavior of a base course aggregate. Based on the simulation results, the benefits of the wicking geotextile have been comprehensively discussed. To further incorporating the benefits into the pavement designs, the methodologies of determining the effective resilient modulus were first discussed. Then, two calculation examples were presented to demonstrate how the modulus will be used in the design guidelines.

7.1 Determination of Effective Resilient Modulus

In the AASHTO (1993) design guide, the effective soil resilient modulus was proposed to account for the seasonal modulus variations and this definition was adopted by Guo (2019) and in this paper. The effective resilient modulus was defined as the equivalent modulus that would result in the same damage when considering the seasonal modulus variations. Based on this definition, the predicted total traffic repetitions based on effective resilient modulus should be the same as the allowable traffic repetitions determined by actual resilient modulus values (Huang 1993). Firstly, based on the proposed numerical model, the daily resilient modulus values of the base course were determined. Secondly, to obtain a more representative monthly resilient modulus value, the daily relative damage ratio, uf, was determined according to Equation 17a. Thirdly, the monthly average damage ratio was determined based on the ratio of the cumulative damage over the number of days in that month, as expressed in Equation

17b. Fourthly, the monthly effective resilient modulus was back-calculated according to Equation 17c. Finally, the annual effective resilient modulus was obtained by repeating the whole procedures by using the calculated monthly effective resilient modulus as inputs.

$$u_f = 1.18 \times 10^8 M_R{}^{-2.32} \tag{17a}$$

$$\overline{u_f} = \frac{\sum u_f}{n} \tag{17b}$$

$$\bar{M}_R = \sqrt[2.32]{\frac{1.18 \times 10^8}{\overline{u_f}}} \tag{17c}$$

where, u_f = relative damage; M_R = resilient modulus; n = time interval between adjacent modulus values is specified; $\overline{u_f}$ = average relative damage; and $\overline{M_R}$ = effective soil resilient modulus.

It is important to point out that the effective resilient modulus was based on the daily resilient modulus data at the bottom of the base course beneath the center of the tire pressure (critical points). Based on the discussed method, the annual effective resilient modulus values were 66.7 MPa, 64.7 MPa, and 101.0 MPa for Cases I, II and III, respectively. According to Figure 4b, though the soil resilient modulus for Case II was higher than that for Case I in spring and winter times, it suffered a long period of time with lower resilient modulus values in the summertime. Therefore, the calculated annual effective resilient modulus values were very close for Cases I and II. However, due to the existence of the wicking geotextile, the excess water could be drained out of the system and the base course experienced limited saturation in the summer. Therefore, the calculated annual resilient modulus for Case III was the highest among all three cases.

7.2 AASHTO 1993 Design Guideline

This section provides an example to demonstrate how to incorporate the benefits of the wicking geotextile into the AASHTO 1993 design guide. Equation 18 was the design equation for the AASHTO 1993 flexible pavement design.

$$\log(W_{18}) = Z_R S_0 + 9.36 \cdot \log(SN+1) - 0.2 + \frac{\log[\Delta PSI / (4.2 - 1.5)]}{0.4 + 1094/(SN+1)^{5.19}} + 2.32 \cdot \log(M_R) - 8.07$$

(18)

where W_{18} = number of 80-kN (18-kip) equivalent single axle loads (ESALs), Z_R = design reliability level, S_0 = overall design uncertainty level, ΔPSI = allowable serviceability loss at the end of design, SN = structural number, and M_R = resilient modulus of the underlying pavement layer.

Assuming a flexible pavement was designed for 30 years and designed traffic was 11.6 million ESALs. The designed reliability of the pavement was 90%, and the corresponding Z_R and S_0 values were -1.282 and 0.45, respectively. The ΔPSI was 1.7 and the subgrade resilient modulus was 45.2 MPa (6556 psi) for all the simulated cases. Given the design parameters and introducing to Equation 18, the calculated structure number was 5.3. Note that since the subgrade soil was assumed to be the same for all cases, the required overall structure number was also the same. The next step was to determine the structure number of each pavement layers based on layer properties. The structural number, SN, was a function of layer thickness, layer coefficients, and drainage coefficients, as expressed in Equation 19 (Huang 1993). Van Til (1972) proposed the empirical equations to determine the layer coefficient of dense-graded AC based on modulus values. The required structural number for the AC layer could be determined by using Equation 18 with M_R to be the effective resilient modulus of the granular base course, $\overline{M}_R$, and assuming the drainage coefficient of the base course, m_2, to be 1.0. Then the required structural number for the AC layer, SN_1, could be solved. For this paper, since the modulus of the AC layer was constant (refer to Table 1), the corresponding layer coefficient of the AC layer, a1, was calculated as 0.26 for all cases. It’s noted that this calculated value is smaller than a typical value of layer coefficient of a dense graded AC layer.

$$SN = a_1 D_1 + a_2 D_2 m_2 \tag{19}$$

$$a_2 = 0.249 \cdot \log(\overline{M}_R) - 0.977 \tag{20}$$

where SN = structural number, a_1 and a_2 = layer coefficients for the AC layer and base course, m_2 = drainage coefficient for the base course, D_1 and D_2 = layer thicknesses for the AC layer and base course, and $\overline{M_R}$ = effective resilient modulus of the base course.

Equation 20 gives the empirical equation to determine the layer coefficient of the base course. Note that the effective resilient modulus for each case was different due to different treatments for the pavement system. In addition, the improved pavement performance due to the installation of geotextiles was considered in terms of improved resilient modulus values. Based on the overall structure number (5.3) and the required structural number of the AC layer (SN_1), the required structural number (SN_2) and the thickness (D_2) of the base course could be determined as expressed in Equation 21.

$$\begin{aligned} SN_2 &= SN - SN_1 \\ D_2 &= SN_2 / a_2 m_2 = (SN - SN_1) / a_2 m_2 \end{aligned} \tag{21}$$

The benefits of the reinforced pavement design could be reflected in terms of the Base Course Thickness Reduction (BCR) ratio (Berg et al. 2000). For this paper, Case I served as a control case, representing the pavement performance without any treatment and the corresponding base course thickness, $D_{2,control}$, could be calculated according to Equation 21. Similarly, the thickness of the base course for Case III, $D_{2,wick}$, could be determined the same way described above. Then, the BCR ratio could be determined by comparing the difference in the required base course thickness, expressed as in Equation 22.

$$D_{2,wick} = D_{2,control} \times (1 - BCR) \tag{22}$$

where $D_{2,control}$ and $D_{2,wick}$ = base course thicknesses for pavement without and with the wicking geotextile, and BCR = base course reduction ratio.

Thus, the benefits of the wicking geotextile could be incorporated into the AASHTO 1993 design guide. Based on the presented method, the required parameters during the calculations have been summarized in Table 3. It is important to point out that the values presented in Table 3 do not necessarily represent an actual field condition. Table 3 only aims at demonstrating and comparing the thicknesses of a base course with different treatments. The thicknesses of the base course for Cases I, II, and III were 1.1 m, 1.3 m, and 0.6 m, respectively and the corresponding BCR values for G1 and G2 were -16.8% and +48.8%, respectively. It's noted that the thicknesses for Cases I to III were much higher than the actual field condition. Van Til et al. (1972) proposed Equation 20 to estimate the layer coefficient of an untreated base course from its resilient modulus. For example, the layer coefficient of a base course is 0.14 for a resilient modulus of 207 GPa (30,000 psi). However, in this paper, the authors used the effective resilient modulus value, which was the weighted modulus value throughout a year. The effective resilient modulus values ranged from 64 MPa to 101 MPa, resulting in much smaller layer coefficient values. Given the same layer coefficient for a base course, one is expected to obtain a much larger thickness value. To determine the actual thickness of the base course, one need to obtain the calibrated parameters that account for the effects of local climate conditions and material properties. Again, the results presented here were only for demonstrative purposes. The results indicated that the reinforcing benefit of the non-wicking geotextile was devastated due to the capillary break effect and excess water accumulation at the soil-geotextile interface. Field observations (Clough and French 1982; Richardson 1997) already validated the simulation results. In comparison, the wicking geotextile could provide superior lateral drainage ability which could efficiently drain the excess water out of pavement structures. Based on the AASHTO design guide, the thickness of the base course could be reduced by 48.8%.

Table 3. Comparisons of Pavement Performance Based on AASHTO 1993 Design Guide

Case	Treatment	Effective Resilient Modulus M_R	Layer Coefficient a_2	Structural Number SN_2	Base Course Thickness D_2	Base Course Reduction *BCR*
		(MPa)	-	-	(m)	(%)
I	-	66.7	0.015	0.65	1.1	-
II	G1 (non-wicking Geotextile)	64.7	0.012	0.7	1.3	-16.3
III	G2 (Wicking Geotextile)	101.0	0.060	1.41	0.6	+48.8

7.3 MEPDG Design Guideline

As mentioned in the previous section, the effect of seasonal variations was considered in the procedure of determining the effective resilient modulus. Therefore, when choosing the material input for the unbounded base course, level 3 was selected and the effective resilient modulus was entered that was held constant throughout the entire year. Meanwhile, the enhanced integrated climate model (EICM) module embedded in the design guide software was also disabled. To better observe the differences in pavement performance caused by seasonal variations of base course resilient behavior, the inputs for each case were the same except for the value of effective resilient modulus of the base course. The design life of the new pavement was 30 years and the pavement structure was the same as demonstrated in Figure 2a, with a 0.1 m-thick AC layer, a 0.4 m-thick base course, and a semi-infinite deep subgrade. The air voids and Poisson’s ratio for the asphalt mixture were assumed to be 4% and 0.3, respectively. The thermal conductivity and heat capacity of the AC layer were 0.96 KJ/kg/ºC and 1.16 W/m/ºC, respectively. The water table was assumed to be at 1.0 m below the ground level. The values for traffic and climate inputs were selected to be the default values and the ID for the weather station was 139530. Again, the authors realize that the performance models of the ME approach were based on the LTPP database, which was developed through real vehicle loading and measurements made in different climatic zones. The following discussion was merely based on the same properties of the AC and the results did not indicate the actual pavement performance. The purpose of the comparison was to evaluate and quantify the benefits of the wicking geotextile given the same climate condition and the same AC properties.

Part of the simulation outputs are presented as shown in Figure 13 and summarized in Table 4. Figure 17a shows the predicted total rutting depths for Cases I-III, which were calculated based on the empirical equations and were the summation of the rutting in each sublayer. Due to the similarities of the inputs for Cases I and II, the total rutting curves were very close to each other and the values were 19.7 mm and 19.9 mm, respectively. In comparison, the effective resilient modulus of te base course was 101 MPa due to the existence of the wicking geotextile, resulting in a smaller total rutting depth value of 13.3 mm at the end of the 30 years design life. By using the wicking geotextile, the total rutting depth was reduced by 35% compared with the control case. In addition, the alligator cracking, also known as the bottom-up cracking, was often observed along the wheel paths. If the stiffness of the base course was relatively weak, the severity of alligator cracking was expected to be high. Figure 17b presents the percentage of alligator cracking with time during the 30 years design life. Similar to the total rutting curves in Figure 17a, the percentages of alligator cracking for Cases I and II were higher than that for Case III. However, since alligator cracking was also dependent on the properties of the AC layer. The differences in alligator cracking were not too obvious, with the highest value of 95.4% for Cases I and II and the lowest value of 91.0% for Case III.

Table 4. Comparisons of Pavement Performance Based on AASHTOWare Pavement ME Design Guide

Case	Treatment	Effective Resilient Modulus M_R	AC	Subgrade	Total Rutting	Alligator Cracking
		(MPa)			(mm)	(%)
I	-	66.7	SuperPave 76-22, M_R = 1GPa	CBR= 4%, M_R=45.2 MPa	20	95.4
II	G1 (non-wicking Geotextile)	64.7			20	95.4
III	G2 (Wicking Geotextile)	101.0			13	91.0

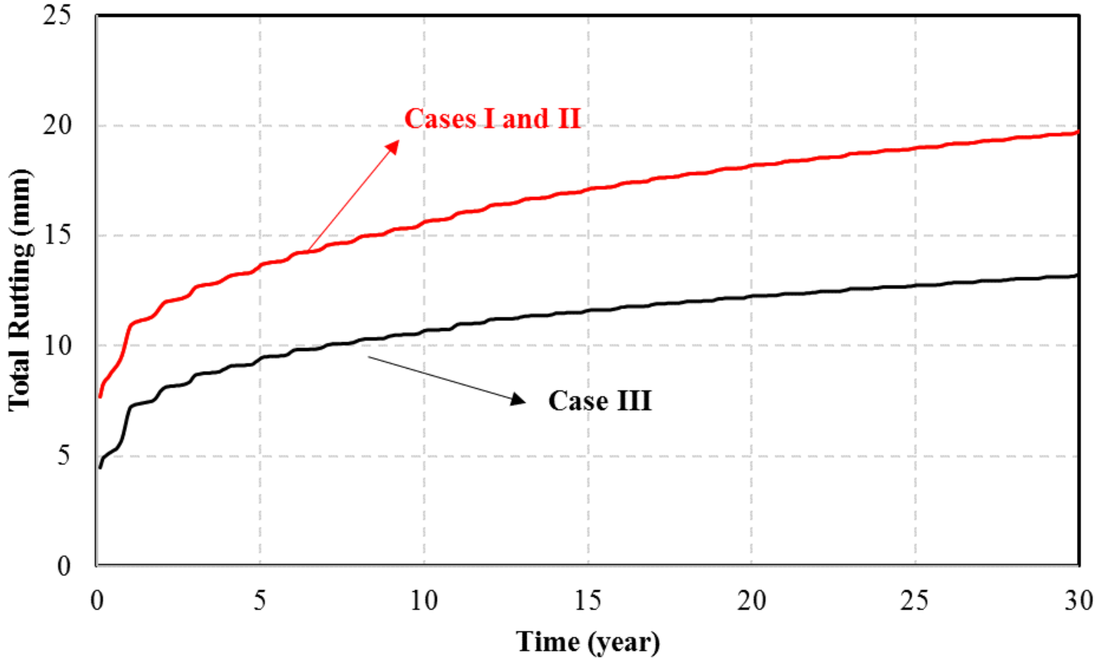

(a)

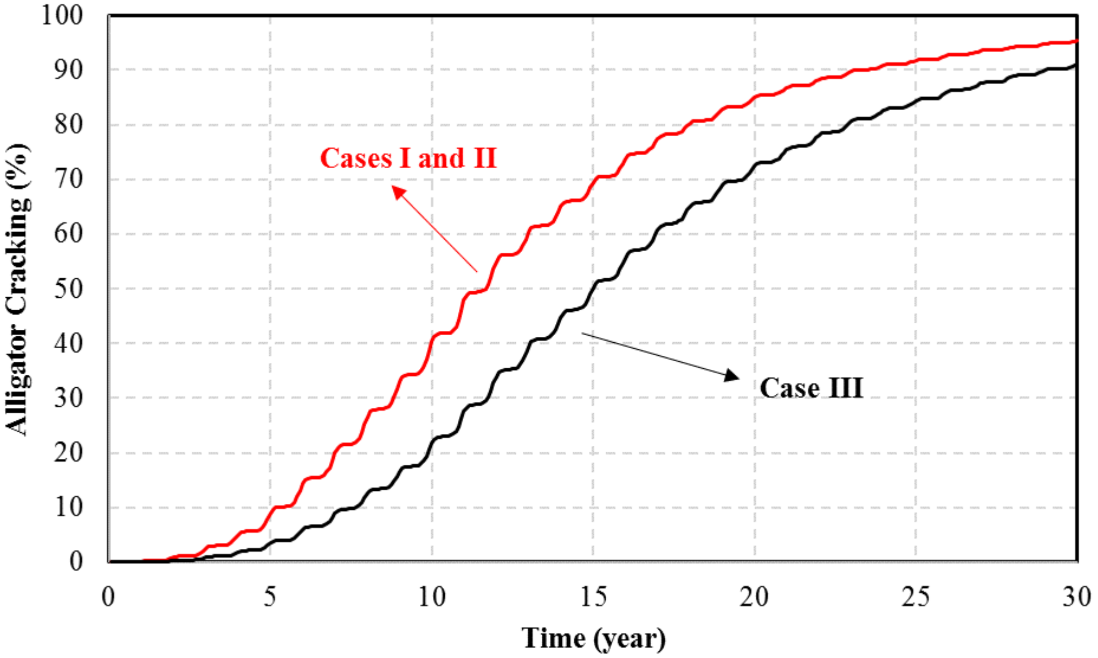

(b)

Figure 17 Selected AASHTOWare Pavement ME Design Software Outputs. (a) total rutting, and (b) alligator cracking.

Chapter. 8 Conclusions

This study aimed at predicting the seasonal variations of the resilient behavior of a base course under localized climatic conditions. A coupled hydro-mechanical model with considerations of climatic effect was proposed to evaluate interactions between the soil mass and the ambient environment. Numerical simulations were performed to evaluate the dynamic performance of a pavement structure under different working conditions. Based on simulation results, the major conclusions are summarized as follows:

1. The proposed coupled hydro-mechanical model with considerations of climatic effect can be used to predict the seasonal variations of the resilient behavior of the base course. The proposed model is suitable for saturated and unsaturated soils and is able to evaluate the interactions between the pavement structure and the ambient environment

2. For a new flexible pavement with a shallow groundwater table (Case I), the major detrimental factor affecting the resilient behavior of a base course was capillary action. The resilient modulus distribution was highly nonlinear and would reduce to a quarter of the designed value. Therefore, the resilient modulus of the base course was sensitive to water content variations.

3. The influence of rainfall duration was more significant than rainfall intensity in reducing the soil resilient modulus. For longer duration rainfall events, more water will be infiltrated into the pavement foundation and the corresponding resilient modulus would be lower. In contrast, if the rainfall intensity was high, most of the water would runoff rather than infiltrating into the pavement foundation, the reduction in resilient modulus was not significant as that in rainfall events with longer durations. The precipitation and evapotranspiration data served as the lower and upper limit for soil water storage and played important roles in keeping the water balance within the grass root zone.

4. The post-construction water content of the base course could not be maintained at the designed value of 8.5%. Based on the simulation results, the water content increased to about 10.0% and the corresponding resilient modulus decreased to 33% compared with the value at the optimum water content.

5. Non-wicking geotextiles resulted in excess water accumulation at the soil-geotextile interface due to the capillary break effect. The excess water significantly devastated the reinforcing benefits and the calculated effective resilient modulus was even lower than the controlled case. That is to say, non-wicking geotextiles were not recommended to be used in a condition with a shallow water table. In comparison, due to the superior lateral drainage ability of the wicking geotextile, the excess water could be drained out of pavement structures efficiently. The effective resilient modulus of the baes course was increased by 51% compared with the controlled case.

6. This paper adopted a methodology to incorporate the benefits of both non-wicking and the wicking geotextile into the AASHTO 1993 and MEPDG design guides. Based on this method, the thickness of the base course could be reduced by 48.8% and the rutting depth could be reduced by 35% if the wicking geotextile was installed, respectively.

References

AASHTO (1993). “Guide for design of pavement structures, 1993.” AASHTO, Washington, DC.

AASHTO (2003). “Standard method of test for resilient modulus of subgrade soils and untreated base/subbase materials.” AASHTO T309-99. Washington, DC.

AASHTO (2008). “Mechanistic-empirical pavement design guide-a manual of practice.” AASHTO, Washington, DC.

Abaqus, V. (2014). “6.14 Documentation.” Dassault Systemes Simulia Corporation.

Allen, R. G., Pereira, L. S., Raes, D., and Smith, M. (1998). “Crop evapotranspiration-guidelines for computing crop water requirements-FAO Irrigation and drainage paper 56.” FAO, Rome, 300(9), D05109.

ARA (2004). “Guide for mechanistic-empirical design of new and rehabilitated pavement structures.” Final Report, NCHRP Project 1-37A.

ASTM D2487 (2011). “Standard Practice for Classification of Soils for Engineering Purposes (Unified Soil Classification System).” ASTM International, West Conshohocken, PA. https://doi.org/10.1520/D2487-17.

ASTM D420-18 (2018). “Standard Guide for Site Characterization for Engineering Design and Construction Purposes.” ASTM International, West Conshohocken, PA, https://doi.org/10.1520/D0420-18.

ASTM D4694-09 (2015). “Standard Test Method for Deflections with a Falling-Weight-Type Impulse Load Device.” ASTM International, West Conshohocken, PA, https://doi.org/10.1520/D4694-09R15.

Biot, M. A. (1941). “General theory of three-dimensional consolidation.” Journal of applied physics, 12(2), 155-164.

Brutsaert, W. (2013). Evaporation into the atmosphere: theory, history and applications, Springer Science & Business Media.

Cedergren, H. R. (1974). “Drainage of highway and airfield pavements.” Transportation Research Record: Journal of the Transportation Research Board.

Christopher, R.B., Schwartz, C., and Boudreau, R. (2010). “Geotechnical aspects of pavements: reference manual.” FHWA NHI-05-037, Federal Highway Administration, Washington, DC.

Dempsey, B.J., Herlach, W.A., and Patel, A.J. (1985). “The climatic-materials-structural pavement analysis program." FHWA/RD-84-115, 3, Federal Highway Administration, Washington, DC.

Elsayed, A., and Lindly, J. (1996). "Estimating permeability of untreated roadway bases." Transportation Research Record: Journal of the Transportation Research Board, 1519, 11-18.

Fredlund, D., and Morgenstern, N. (1976). "Constitutive relations for volume change in unsaturated soils." Canadian Geotechnical Journal, 13(3), 261-276.

Fredlund, D.G., Rahardjo, H, and Fredlund, M.D. (2012). Unsaturated soil mechanics in engineering practice. John Wiley & Sons, Hoboken, NJ.

Gray, D. M. (1970). "Handbook on the principles of hydrology: with special emphasis directed to Canadian conditions in the discussions, applications, and presentation of data." Canadian National Committee for the International Hydrological Decade.

Guymon, G.L., Berg, R.L., and Johnston, T.C. (1986). "Mathematical model of frost heave and thaw settlement in pavements." U.S. Army Cold Regions Research and Engineering Laboratory (CRREL), Hanover, New Hampshire.

Harichandran, R., Baladi, G., and Yeh, M. (1989). "Development of a computer program for the design of pavement systems consisting of bound and unbound materials." Department of Civil and Environmental Engineering, Michigan State University.

Henry, K. S., and Holtz, R. D. (2001). "Geocomposite capillary barriers to reduce frost heave in soils." Canadian Geotechnical Journal, 38(4), 678-694.

Huang, Y. H. (2004). Pavement analysis and design. Prentice Hall, Upper Saddle River, NJ.

Kunze, R. J., Uehara, G., and Graham, K. (1962). "Factors important in the calculation of hydraulic conductivity." Soil Science Society of America Journal, 32(6), 760-765.

Larson, G., and Dempsey, B.J. (1997). "Enhanced integrated climatic model, version 2.0, final report." Contract DTFA MN/DOT 72114, Department of Civil Engineering, University of Illinois at Urbana-Champaign, Urbana, IL.

Leung, A.K., Garg, A., and Ng, C.W.W. (2015). "Effects of plant roots on soil-water retention and induced suction in vegetated soil." Engineering Geology, 193, 183-197.

Li, L., Liu, J., Zhang, X., and Saboundjian, S. (2011). "Resilient modulus characterization of Alaska granular base materials." Transportation Research Record: Journal of the Transportation Research Board, 2232, 44-54.

Lin, C., Zhang, X., and Han, J. (2018). "Comprehensive material characterization of pavement structure installed with wicking fabrics." Journal of Materials in Civil Engineering, 31(2), 04018372.

Liu, S.J., and Lytton, R.L. (1985). “Environmental effects on pavement drainage”. FHWA-DTFH61-87-C-00057, Federal Highway Administration, Washington, DC.

Miller, E. (1953). “THE WASHO ROAD TEST.” Highway Res Abstracts Hwy Res Board.

Morton, F. (1975). “Estimating evaporation and transpiration from climatological observations.” Journal of Applied Meteorology, 14(4), 488-497.

Raad, L., and Figueroa, J. L. (1980). “Load response of transportation support systems.” Journal of Transportation Engineering, 106(1).

Richter, C.A. (2006). “Seasonal variations in the moduli of unbound pavement layers.” FHWA-HRT-04-079, Federal Highway Administration, Washington, DC.

Ridgeway, H. H. (1982). “Pavement subsurface drainage systems.” NCHRP synthesis of highway practice 96.

Roberson, R., and Siekmeier, J. (2002). “Determining material moisture characteristics for pavement drainage and mechanistic-empirical design.” Research Bulletin, Minnesota Department of Transportation, Office of Materials and Road Research.

Romero, C.C., and Michael D.D. (2016). “Review of turfgrass evapotranspiration and crop coefficients.” Transactions of the ASABE, 59(1), 207-223.

Shahin, M.Y. (1994). Pavement Management for Airports, Roads and Parking Lots. Kluwer Academic Publishers, Dordrecht, Hardbound.

Tran, D. T., Fredlund, D. G., and Chan, D. H. (2015). “Improvements to the calculation of actual evaporation from bare soil surfaces.” Canadian Geotechnical Journal, 53(1), 118-133.

Uzan, J., Witczak, M. W., Scullion, T., and Lytton, R. L. (1992). “Development and validation of realistic pavement response models.” In International Conference on Asphalt Pavements, 7th, 1992, Nottingham, United Kindom.

Van Sambeek, R. J. (1989). “Synthesis on subsurface drainage of water infiltrating a pavement structure.” No. MN/RC-89/20, Braun Pavement Technologies.

Wilson, G. W., Fredlund, D., and Barbour, S. (1994). “Coupled soil-atmosphere modeling for soil evaporation.” Canadian Geotechnical Journal, 31(2), 151-161.

Wilson, G.W. (1997). “Surface fluxes for geotechnical engineering problems.” Ph.D. Dissertation, University of Saskatchewan, Saskatoon, SK.

Wilson, G.W., Fredlund, D.G., Barbour, S.L., and Pufahl, D.E. (1997). “The use of ground surface moisture flux boundary conditions in geotechnical engineering.” In Proceeding of the

International Conference on Soil Mechanics and Foundation Engineering, AA, Balkema, 3, 1861-1864.

Witczak, M.W., Andrei, D., and Houston, W.N. (2000). “Resilient modulus as a function of soil moisture – summary of predictive models.” Development of the 2002 Guide for the Development of New and Rehabilitated Pavement Structures, NCHRP 1-37A, Inter Team Technical Report (Seasonal 1-4), Tempe, Arizona.

WRCC (2017). <https://raws.dri.edu/>. (latest access on June 15, 2018)

Wyatt, T., Barker, W., and Hall, J. (1998). “Drainage Requirements in Pavements User Manual.” FHWA-SA-96-070, Federal Highway Administration, Washington, DC.

Zhang, X., and Liu, J. (2008). “Numerical simulation of the influence of climatic factors on concrete pavements built on expansive soil.” GeoCongress 2008: Geosustainability and Geohazard Mitigation, 554-561.

Zhang, X., Lytton, R., and Briaud, J. (2005). "Coupled consolidation theory for saturated-unsaturated soils." Proc., Proc., 3rd Biot Conf. on Poromechanics (Biot Centennial), Univ. of Oklahoma, 323-330.